Monthly Notices
of the
ROYAL ASTRONOMICAL SOCIETY

MNRAS **460,** 4417–4432 (2016)
Advance Access publication 2016 May 30

doi:10.1093/mnras/stw1282

The X-ray spectral evolution of the ultraluminous X-ray source Holmberg IX X-1

Wasutep Luangtip,[1,2]★ Timothy P. Roberts[1] and Chris Done[1]

[1]*Centre for Extragalactic Astronomy, Department of Physics, University of Durham, South Road, Durham DH1 3LE, UK*
[2]*Department of Physics, Faculty of Science, Srinakharinwirot University, 114 Sukhumvit 23, Wattana, Bangkok 10110, Thailand*

Accepted 2016 May 26. Received 2016 May 26; in original form 2015 September 24

ABSTRACT

We present a new analysis of X-ray spectra of the archetypal ultraluminous X-ray source (ULX) Holmberg IX X-1 obtained by the *Swift*, *XMM–Newton* and *NuSTAR* observatories. This ULX is a persistent source, with a typical luminosity of $\sim 10^{40}$ erg s^{-1}, that varied by a factor of 4–5 over eight years. We find that its spectra tend to evolve from relatively flat or two-component spectra in the medium energy band (1–6 keV), at lower luminosities, to a spectrum that is distinctly curved and disc-like at the highest luminosities, with the peak energy in the curved spectrum tending to decrease with increased luminosity. We argue that the spectral evolution of the ULX can be explained by super-Eddington accretion models, where in this case we view the ULX down the evacuated funnel along its rotation axis, bounded by its massive radiatively driven wind. The spectral changes then originate in enhanced geometric beaming as the accretion rate increases and wind funnel narrows, causing the scattered flux from the central regions of the supercritical flow to brighten faster than the isotropic thermal emission from the wind, and so the curved hard spectral component to dominate at the highest luminosities. The wind also Compton down-scatters photons at the edge of the funnel, resulting in the peak energy of the spectrum decreasing. We also confirm that Holmberg IX X-1 displays spectral degeneracy with luminosity, and suggest that the observed differences are naturally explained by precession of the black hole rotation axis for the suggested wind geometry.

Key words: accretion, accretion discs – black hole physics – X-rays: binaries – X-rays: individual: Holmberg IX X-1.

1 INTRODUCTION

Ultraluminous X-ray sources (ULXs) are extragalactic, non-nuclear point sources, with X-ray luminosities $>10^{39}$ erg s^{-1}, equivalent to or in excess of the Eddington limit for 10 $M_\odot$ black holes (BHs; see Roberts 2007; Feng & Soria 2011 for reviews). Given their non-nuclear locations, they cannot be powered by accretion on to the central supermassive BH of their host galaxy. However, due primarily to their extreme luminosities, it has been proposed that ULXs might be a hitherto missing class of massive BHs, the intermediate mass black holes (IMBHs), with $10^2 < M_{\rm BH} < 10^5$ (e.g. Colbert & Mushotzky 1999; Miller et al. 2003), that accrete material at the sub-Eddington rates we typically see in Galactic black hole binaries (BHBs). Indeed, some of the most luminous ULXs remain good candidates for sub-Eddington accretion on to IMBHs, for instance HLX-1 in ESO 243-49 (Farrell et al. 2009) and a sample of the most extreme ULXs discussed by Sutton et al. (2012), including NGC 2276 3c (Mezcua et al. 2015). However, recent mass constraints on two ULXs (Liu et al. 2013; Motch et al. 2014) suggest the presence of stellar mass BHs (sMBHs) in these objects, that must be accreting at super-Eddington rates. These results, combined with differences in both the X-ray spectral and timing characteristics of many ULXs when compared to sub-Eddington BHBs (e.g. Gladstone, Roberts & Done 2009; Sutton, Roberts & Middleton 2013), indicate that this could be the nature of most ULXs, although an intriguing possibility is that some ULXs may harbour larger stellar remnant BHs (MsBHs, $20 < M_{\rm BH} < 100$) that may form in metal-poor environments (e.g. Zampieri & Roberts 2009). Similarly, we now know that at least one ULX harbours an extreme super-Eddington neutron star, given the detection of pulsations from an object in M82 (Bachetti et al. 2014).

The X-ray spectra of ULXs have been widely studied since the launch of the *XMM–Newton* and *Chandra* X-ray observatories, and so knowledge of their typical properties has grown substantially in the last decade. It has been shown that the X-ray spectra of ULXs in the 0.3–10 keV band are composed of two individual components: one dominating at energies below 1 keV (the soft excess)

★ E-mail: wasutep@g.swu.ac.th

and another dominating at photon energies above 2 keV (the hard component; e.g. Miller et al. 2003). The very cool temperatures ($\lesssim$0.2 keV) obtained when fitting the soft excess with accretion disc models were initially used to imply the existence of IMBHs in many bright ULXs (e.g. Miller, Fabian & Miller 2004). However, subsequent studies of the highest quality X-ray spectra of ULXs (Stobbart, Roberts & Wilms 2006; Gladstone et al. 2009) demonstrated that the hard component turns over at photon energies ∼3–7 keV, a result that has more recently been confirmed by broad-band *NuSTAR* observations that show this break extends well above 10 keV (Bachetti et al. 2013; Walton et al. 2014). This spectrum is not generally observed in Galactic BHBs, which when combined with the high luminosities of ULXs implies it is likely to represent a new mode of accretion – putatively called the *ultraluminous state* – in which sMBHs are accreting material at super-Eddington rates (Gladstone et al. 2009).

A physical scenario that could describe super-Eddington accretion processes has been discussed by several theoretical and simulation-based works (see e.g. Poutanen et al. 2007; Kawashima et al. 2012; Takeuchi, Ohsuga & Mineshige 2013, 2014; Sądowski & Narayan 2016)[1]. At super-Eddington rates accreting BHs are predicted to increase their disc scaleheight (H/R) to ∼ unity as the disc interior becomes advection-dominated and so heats up; the outer layers of the disc then become loosely bound, and the intense radiation release from the disc launches a massive, outflowing wind within a photospheric radius, that forms a funnel-like structure around the rotational axis of the BH. Observational support for this scenario has been gradually emerging over the last few years. Sutton et al. (2013) showed that the good quality spectra of ULXs observed by *XMM–Newton* predominantly appear like broadened discs at luminosities below $\sim 3 \times 10^{39}$ erg s^{-1}, where an sMBH would be accreting material at ∼ the Eddington rate; above this luminosity, the ULXs accrete material at rates that may substantially exceed Eddington, and the spectra become two component, as described above. The harder component is well-modelled by an optically thick Comptonizing corona ($kT_e \sim 2$ keV, $\tau \sim 10$; see e.g. Vierdayanti et al. 2010; Pintore & Zampieri 2012); however, recent works have interpreted this spectrum as more likely to originate in emission from the hot, inner parts of the accretion flow (e.g. Middleton et al. 2011; Kajava et al. 2012). The soft, disc-like component is then interpreted as emission from the optically thick and massive outflowing disc wind (e.g. Kajava & Poutanen 2009, although see Miller et al. 2013).

This interpretation is strongly supported by work considering the spectral and temporal variability properties of ULXs, where very high levels of flux variability on time-scales of $\lesssim$ 100 s of seconds are associated with the hard spectral component when the spectrum is dominated by the soft component (i.e. the ULX is in a soft ultraluminous, or SUL, regime; Sutton et al. 2013). This can be explained by the wind being an inhomogeneous medium, where optically thick clumps pass through the observer's line of sight to the central regions of the accretion flow and scatter away the hard photons (Middleton et al. 2011, 2015a; Sutton et al. 2013). That this variability is seen when the spectrum is in the SUL regime supports the notion that both accretion rate and viewing angle dictate the observational appearance of ULXs; in the SUL regime the line-of-sight intersects the wind, which diminishes the hard component, and adds extrinsic variability. In contrast, when viewed down the funnel, a hard ultraluminous (HUL) spectrum is observed, with little or no strong variability. The major missing piece of the puzzle in this model is a direct detection of the wind material, from absorption or emission lines in the optically thin phase of the wind that must be present as the wind diffuses away from the disc; but this may be the origin of residuals in the soft X-ray spectra of ULXs (Middleton et al. 2014), and broad emission lines seen in the optical spectra of ULX counterparts (Fabrika et al. 2015).

Holmberg IX X-1 is a nearby ULX ($d = 3.42$ Mpc; Liu & Bregman 2005) located close to the dwarf galaxy Holmberg IX. It is a persistent source with luminosity $\sim 10^{40}$ erg s^{-1} that displays variations in flux by a factor of 3–4 on time-scales of days (Kaaret & Feng 2009; Kong et al. 2010). The source was first discovered by the *Einstein* Observatory (Fabbiano 1988) and has been well studied over the past 30 yr due to its proximity and so high X-ray flux. Despite some initial uncertainty in its nature, with some discussion as to whether it was a background QSO or a supernova remnant, it was confirmed as a likely ULX at the start of the *XMM–Newton* and *Chandra* epoch (La Parola et al. 2001). Subsequent studies focusing on the high-quality spectra obtained by *XMM–Newton* have shown that they are typical of a ULX in the HUL regime (e.g. Stobbart et al. 2006; Sutton et al. 2013), and a study of its X-ray spectral variability by Vierdayanti et al. (2010) showed that the variability was not a simple function of luminosity, but that subtle variations occurred that appeared independent of accretion rate. A more recent study incorporating broad-band (0.3–30 keV) spectra from *NuSTAR* demonstrated that the spectra can be explained by two optically thick thermal components, similar to the spectra seen in the 0.3–10 keV range; furthermore the spectral evolution was explored, with its characteristics hypothesized to be indicative of physical changes in the highly dynamical, outflowing wind or the evolution of the hot inner region of the disc itself (Walton et al. 2014). Given its high flux and hard spectrum, Holmberg IX X-1 was a natural choice to search for absorption/emission features in the Fe K band that may be indicative of material in an outflowing wind. However, none were found to stringent limits by Walton et al. (2013a); this is perhaps unsurprising, though, given the HUL spectra that are indicative of Holmberg IX X-1 being viewed down the funnel in its disc/wind structure, rather than through its wind.

Although we now have a provisional working model for the super-Eddington processes that occur in ULXs, much of the detail remains to be determined. One obvious way of better assessing the physical mechanisms and/or geometry at play in ULXs is through the detailed study of bright, individual archetypes for the class. In this work, we analyse the variation in spectra of Holmberg IX X-1 using data obtained from the *Swift*, *XMM–Newton* and *NuSTAR* X-ray observatories, in order to constrain the spectral evolution of the ULX with luminosity, and so better determine its physics. The paper is laid out as follows. In Section 2, we explain how we select the X-ray data, how we reduce it and how we create the ULX spectra. The details of the spectral analysis are presented in Section 3 and we discuss what we learn from the variability of the spectra in Section 4. Our findings are summarized in Section 5.

2 OBSERVATIONS AND DATA REDUCTION

2.1 *Swift* data

The X-ray variability of Holmberg IX X-1 has been monitored intermittently by *Swift* during the last decade, some observations of which were part of a monitoring programme for bright ULXs (e.g. Kaaret & Feng 2009). We searched for useful *Swift* observations

[1] Although other models may not be discounted based on current data, for example locally inhomogeneous discs (Miller et al. 2014).

Table 1. *XMM–Newton* observations of Holmberg IX X-1.

ObsID	Obs. date	PN/M1/M2 Exp.[a] (ks)	Total counts[b]	θ[c] (arcmin)	References[d]
0111800101[e]	2001-04-22	–/76.0/76.7	65 072	10.70	1,2,3,4,5,6,7,8
0111800301[f]	2001-04-22	–	–	10.70	–
0112521001	2002-04-10	5.9/9.5/9.9	24 138	2.09	1,2,3,6,8,9,10,11,12,13,16
0112521101	2002-04-16	7.2/8.6/8.5	29 409	2.09	2,3,6,9,10,11,12,13,14,15,16
0200980101	2004-09-26	38.0/62.2/65.0	125 946	2.18	1,2,3,4,5,6,7,9,10,11,12,16,17,18,19,20,21
0657801601[f]	2011-04-17	–	2634	4.50	11,22,23
0657801801	2011-09-26	3.6/10.8/13.3	28 676	4.50	2,11,16,22,23
0657802001	2011-03-24	2.5/4.7/4.6	7154	4.50	2,11,16,22,23
0657802201	2011-11-23	11.7/15.3/15.2	60 861	4.50	2,11,16,22
0693850801[g]	2012-10-23	5.7/7.8/8.0	24 553	2.17	24
0693850901[g]	2012-10-25	4.9/8.3/11.1	28 040	2.17	24
0693851001[g]	2012-10-27	3.9/5.3/6.5	21 282	2.17	24
0693851101[h]	2012-11-16	2.5/4.4/4.4	24 115	2.17	24
0693851701[h]	2012-11-12	6.1/9.3/9.0	50 831	2.17	24
0693851801[h]	2012-11-14	6.6/8.5/8.5	51 356	2.17	24

Note. [a]The good exposure times obtained from the PN, MOS1 and MOS2 detectors. [b]The total useful counts from the source, observed during the good exposure times, from a combination all three EPIC detectors. [c]The off-axis angle of the source (measured from the EPIC aim point). [d]References to previous studies of this ULX using the pertinent data. These are: (1) Winter, Mushotzky & Reynolds (2007); (2) Sutton, Done & Roberts (2014); (3) Miller et al. (2013); (4) González-Martín et al. (2011); (5) Gladstone et al. (2009); (6) Sutton et al. (2013); (7) Caballero-García & Fabian (2010); (8) Winter, Mushotzky & Reynolds (2006); (9) Walton et al. (2012); (10) Kajava & Poutanen (2009); (11) Pintore et al. (2014); (12) Vierdayanti et al. (2010); (13) Wang et al. (2004); (14) Poutanen et al. (2007); (15) Stobbart et al. (2006); (16) Middleton et al. (2015a); (17) Heil, Vaughan & Roberts (2009); (18) Hui & Krolik (2008); (19) Grisé et al. (2011); (20) Dewangan, Griffiths & Rao (2006); (21) Berghea et al. (2013); (22) Sazonov, Lutovinov & Krivonos (2014); (23) Dewangan et al. (2013); (24) Walton et al. (2014). [e]Only MOS spectra are extracted from the observation as the source position falls outside of the PN detector area. [f]We exclude the observation from the analysis as the good exposure time is too low to obtain good quality spectra. [g]The spectra extracted from these observations were stacked together and analysed as epoch 1 in the broad-band spectral analysis. [h]The spectra extracted from these observations were stacked together and analysed as epoch 2 in the broad-band spectral analysis.

of Holmberg IX X-1 in the *Swift* data archive catalogue[2], using a cone search with radius of 11 arcmin such that the ULX position is always located within the field of view of the *Swift* X-ray telescope (XRT). Only the data obtained in photon counting mode were selected in order to obtain 2D images of the observations. We also selected only those observations in which the XRT exposure time is > 40 s, in order to (typically) obtain at least 10 photon counts from the ULX in each observation. After this step, we ended up with 514 useful observations: 132 observations in which the ULX position lies within a circular region of 5 arcmin radius centred on the XRT detector aim point (hereafter on-axis observations); and a further 382 observations that are *Swift* monitoring observations of the nearby galaxy M81, in which the ULX position is > 5 arcmin from the XRT detector aim point (hereafter off-axis observations) but still lies with in the field of view of the XRT.

We reduced all selected observations of Holmberg IX X-1 following the *Swift* XRT Data Reduction Guide version 1.2.[3] In brief, the raw data were reduced using the script XRTPIPELINE. Using the default parameter values provided by the script, bad pixels were removed and clean event files were created from the good grade events (grade 0–12). Then, source and background spectra were extracted from the clean event files using the script XRTPRODUCTS, which also automatically created the appropriate auxiliary response files (ARFs) and response matrix files (RMFs). In all cases, the source spectra were extracted from a circular region of 47 arcsec radius located at the source position, corresponding to the 90 per cent encircled energy radius at 1.5 keV for the on-axis point spread function (PSF) of the *Swift* XRT[4]. For the background spectra, the extraction was divided into two cases; for the on-axis observations, the background spectra were extracted from an annular region (of inner and outer radii 75 and 150 arcsec, respectively) around the source extraction area; in the case of off-axis observations, we extracted the background spectra from a source free, circular region of radius 150 arcsec next to the source extraction aperture. The properties of the spectra obtained from the *Swift* observations are listed in Table A1.

2.2 *XMM–Newton* data

Holmberg IX X-1 has been observed several times over the last decade-and-a-half by *XMM–Newton*; these observations have been analysed by many authors, as shown in column 6 of Table 1. Here we include all this *XMM–Newton* data in our analysis. We began by searching for observations of the ULX in the *XMM–Newton* data archive[5]; all 15 observations of Holmberg IX X-1 that we found are tabulated in Table 1. We reduced the *XMM–Newton* data using *XMM–Newton* Science Analysis Software (SAS)[6] version 13.5.0, following the instructions in the SAS thread web pages[7]. We reprocessed the observation data files to obtain new calibrated and reprocessed event files, using the scripts EPPROC and EMPROC for the PN and MOS data, respectively. Then, we filtered the event files for background particle flaring events using the SAS task ESPFILT, which generated the clean PN and MOS event files.

[2] http://swift.gsfc.nasa.gov/archive/
[3] http://swift.gsfc.nasa.gov/analysis/xrt_swguide_v1_2.pdf
[4] http://swift.gsfc.nasa.gov/analysis/threads/uvot_thread_spectra.html; note that this decreases to 63 per cent encircled energy for the same radius at 11 arcmin off-axis.
[5] http://nxsa.esac.esa.int
[6] http://www.cosmos.esa.int/web/xmm-newton/download-and-install-sas/
[7] http://www.cosmos.esa.int/web/xmm-newton/sas-threads/

Table 2. *NuSTAR* observations of Holmberg IX X-1.

ObsID	Obs. date	Exp.[a] (ks)	Cnts[b]	Epoch[c]
30002033002	2012-10-26	31.2	13 616	1
30002033003	2012-10-26	88.1	41 967	1
30002033004[d]	2012-11-10	–	–	
30002033005	2012-11-11	40.8	31 450	2
30002033006	2012-11-11	35.2	26 399	2
30002033007[d]	2012-11-14	–	–	
30002033008	2012-11-14	14.5	11 737	2
30002033009[d]	2012-11-15	–	–	
30002033010	2012-11-15	49.0	37 202	2

Note. [a]The good exposure time obtained from each detector. [b]The total counts in each observation, from combining the FPMA and FPMB data. [c]The epoch of observation. The spectra within the same epoch are stacked together and analysed simultaneously (see Section 3.3 for the detail of analysis). [d]We excluded the observation from the analysis as the good exposure time is too low to obtain useful spectral data.

We extracted PN and MOS spectra from the good grade events suggested by the SAS thread, i.e. FLAG = 0 and PATTERN ≤4 for the PN and 12 for the MOS, respectively. The source spectra were extracted from a circular aperture of 50 arcsec radius around the source position, corresponding to ∼90 per cent encircled energy at 1.5 keV of the PN and MOS on-axis PSFs[8]. The background spectra were extracted from a source-free, circular area of 80 arcsec radius near to the ULX, with the same off-axis angle to that of the source and, if possible, from the same CCD as the ULX. The corresponding RMFs and ARFs were generated with the SAS scripts RMFGEN and ARFGEN. The spectra were then grouped to have a minimum of 20 counts per bin to utilize the χ^2 optimization method during spectral modelling. The total number of counts obtained from each *XMM–Newton* observation is shown in column 4 of Table 1.

In the broad-band spectral analysis of the source (Section 3.3), we prepared the *XMM–Newton* spectra using the same method as that of the previous broad-band study of the ULX (Walton et al. 2014). Hence we segregated the *XMM–Newton* spectra that were observed simultaneously with the *NuSTAR* observatory in 2012 October and November into epoch 1 and epoch 2 (see Table 1). The spectra obtained from the same detectors in each epoch were stacked together using the FTOOL ADDSPEC[9], in order to create a single spectrum of PN, MOS1 and MOS2 for each observational epoch. The spectra were then grouped to have a minimum of 50 counts per bin.

2.3 *NuSTAR* data

Holmberg IX X-1 was one of the ULX targets to be observed by *NuSTAR* during the primary mission phase; it was observed simultaneously with *XMM–Newton* in 2012 October and November (see Table 2; Walton et al. 2014). In this work, these public data are also included in our analysis. We reprocessed and reduced the data using the *NuSTAR* data analysis software (NUSTARDAS) version 1.4.1, which is part of the HEASOFT software version 6.16[10], using the *NuSTAR* instrument calibration files (*NuSTAR* CALDB) version 20140414. We extracted the spectra from this data using the wrapper task NUPIPELINE[11], which generated the filtered event files and then extracted the source and background spectra as well as appropriate RMFs and ARFs from the cleaned event and calibration files. The source spectra, all of which were on-axis in the detector, were extracted from a circular aperture of 101 arcsec radius around the source position, corresponding to the 80 per cent encircled energy radius of the *NuSTAR* detector PSF[12]. The background spectra were extracted from a source-free annulus (of inner and outer radius 170 and 270 arcsec, respectively) around the source extraction region.

Similarly to the *XMM–Newton* spectra, we divided the *NuSTAR* spectra into epoch 1 and epoch 2, segregating by the month in which they were observed (see column 5 of Table 2), following the method used in the previous broad-band study of the ULX (Walton et al. 2014). The spectra obtained from the same *NuSTAR* detectors in each epoch were stacked together using the script ADDSPEC, in order to create a single spectrum from the FPMA and FPMB detectors for each observational epoch. Finally, the spectra were grouped to have a minimum of 50 counts per bin.

3 SPECTRAL ANALYSIS AND RESULTS

The large number of X-ray spectra of Holmberg IX X-1, from multiple X-ray missions, provides us with an excellent opportunity to further examine the X-ray spectral evolution of this ULX with luminosity. In this paper, we constrain the shape and hence the evolution of the spectra primarily using a two-component model composed of a multicoloured disc blackbody model (MCD; Mitsuda et al. 1984) and a Comptonizing corona (Titarchuk 1994), i.e. DISKBB + COMPTT in XSPEC. This model, or very similar models, has been used extensively and very successfully to describe ULX X-ray spectra below 10 keV (see e.g. Gladstone et al. 2009; Pintore et al. 2014; Middleton et al. 2015a), with the interesting caveat that the coronae appear cool and optically thick in ULXs modelled in this way ($kT_e \sim$ 1–2 keV; $\tau \gtrsim 5$), most unlike the hot, optically thin coronae seen in Galactic BHBs. We note that there are other empirical models that can produce similar-shaped spectra (see e.g. Stobbart et al. 2006); we do not discuss them in this section, but will return to them later in Section 4 where we use them to illuminate our discussion of the spectral variability.

We simplify the MCD plus Comptonizing corona model by tying the seed photon temperature of the COMPTT component to the temperature of the MCD component in order to get better constraints on the model-fitting parameters. It is noted elsewhere that this simplification may lead to unrealistic values of the seed photon temperature in ULX fits, as the measured MCD temperature might not reflect the true temperature of the seed photons from the inner disc due to the obscuration of this region by the putative optically thick corona (see e.g. Gladstone et al. 2009). However, in this work, we do not attempt to directly interpret the model parameters; instead, we use the model to evaluate the change in the spectral shape, and to attempt to track the relative contributions of the separate soft and hard components of the spectra. So, in our case, the simplification of the model should not overtly affect the interpretation of the spectral evolution.

In fitting models to the spectral data, absorption along the line of sight to Holmberg IX X-1 is accounted for by adding two

[8] https://heasarc.gsfc.nasa.gov/docs/xmm/uhb/offaxisxraypsf.html; this decreases to 43 per cent encircled energy for the same radius at the edge of the detectors.
[9] http://heasarc.gsfc.nasa.gov/ftools/caldb/help/addspec.txt
[10] http://heasarc.gsfc.nasa.gov/docs/software/lheasoft/
[11] https://heasarc.gsfc.nasa.gov/ftools/caldb/help/nupipeline.html
[12] https://heasarc.gsfc.nasa.gov/docs/nustar/NuSTAR_observatory_guide-v1.0.pdf

multiplicative absorption components (TBABS in XSPEC) into the model, using the interstellar abundances reported by Wilms, Allen & McCray (2000). The first absorption component is fixed at 4.06×10^{20} cm^{-2}, and accounts for the Galactic column density along our line of sight (Dickey & Lockman 1990), whilst the second component represents absorption external to our Galaxy, most likely in the immediate vicinity of the ULX and/or in its host galaxy. The spectra were modelled using XSPEC[13] version 12.8.2 over the energy band of 0.3–10 keV (unless otherwise specified). The best-fitting parameters are derived using a χ^2 minimization technique, and throughout this paper their errors are quoted using the 90 per cent confidence interval. We note that the spectral binning changes between different parts of this section (see Sections 2 and 3.1). In the analysis of *Swift* and *XMM–Newton* spectra, we select a minimum counts per bin that is optimized to extract the best constraints from the data available, whilst in the broad-band spectral analysis the spectra are binned to have a minimum of 50 counts per bin in order to replicate the analysis from previous work (Walton et al. 2014).

3.1 *Swift* spectral analysis

3.1.1 Individual spectral analysis

Unfortunately each individual *Swift* spectrum contains insufficient data for detailed spectral analysis (∼10–1000 counts). If we are to obtain the high signal-to-noise (S/N) spectra required for this study, then we must stack *Swift* spectra with similar properties together. A previous spectral study of Holmberg IX X-1 using *Swift* data by Vierdayanti et al. (2010) segregated the spectra into luminosity bins using the detector count rates of the ULX. However, this is not appropriate in this work, as we include off-axis *Swift* spectra, and the observed count rates for a source with a given flux are a function of the detector effective area which varies with off-axis angle (Tagliaferri et al. 2004). For example, the count rate of a source located at 10 arcmin off-axis from the detector aim point is lower by ∼25 per cent than the count rate of the same source located at the detector aim point. Thus, to avoid this issue, we take into account the differences in the detector response by calculating the observed flux of Holmberg IX X-1 in each observation, instead of using the detector count rates. The fluxes were calculated by modelling the individual *Swift* spectra with an absorbed power-law (TBABS*TBABS*POWERLAW in XSPEC), with the absorption modelled as described above.

The 440 spectra in which ≥ 100 counts were detected were grouped to have a minimum of 10 counts per bin, and then each was fitted by the absorbed power-law model. In addition, to include more *Swift* data in the analysis, we also considered another 55 observations which have between 50 and 100 counts. We again grouped the low count spectra to have a minimum of 10 counts per bin, and the spectra were fitted by the absorbed power-law model. However, as these spectra cannot constrain all three model parameters, we froze two – the absorption column external to our Galaxy ($N_{\rm H}$) and the power-law photon index (Γ) – at the average value of the parameters obtained from the best-fitting results of the higher count rate spectra, $\Gamma = 1.6$ and $N_{\rm H} = 3 \times 10^{21}$ cm^{-2}, and we only allowed the normalization to be a free parameter in the fitting. The fitting results of all the individual *Swift* spectra are reported in Table A1 and these were then used as the basis for further spectral analysis.

The light curve of Holmberg IX X-1 obtained from the *Swift* monitoring observations is plotted in Fig. 1. It can be seen that the source flux varied by a factor of 4–5 over a period of eight years. As a first-order analysis of the spectral evolution with time, we plot the photon index of the individual *Swift* spectra as a function of the observing time (bottom panel of Fig. 1); no obvious correlation between the photon index and observation time is evident. To further examine the data, we plot the hardness-intensity diagram in Fig. 2 (where we use the observed 0.3–10 keV flux as a proxy for the intensity, and the photon index for the hardness). Interestingly, the spectra seem to have a bimodal distribution, with one peak at a flux of $\sim 8 \times 10^{-12}$ erg cm^{-2} s^{-1} and the other peak at double this flux ($\sim 1.6 \times 10^{-11}$ erg cm^{-2} s^{-1}). We will consider this further in next section.

3.1.2 Stacked spectral analysis: luminosity segregation

It has been shown in previous studies of ULX spectra (e.g. Stobbart et al. 2006; Gladstone et al. 2009) that their spectral features, particularly the high-energy curvature, are subtle and can only be seen in high quality spectra. So, in order to obtain high S/N *Swift* spectra, we grouped the spectra into appropriate bins and stacked the spectra together to create a single spectrum for each bin, using the following criteria.

We began binning the individual *Swift* spectra using luminosity criteria. In particular, based on the bimodal distribution shown in Fig. 2, we divided the spectra in two main groups demarcated by an observed 0.3–10 keV flux of $\log f_{\rm X} = -10.9$ (in units of erg cm^{-2} s^{-1}), which we refer to hereafter as the low and high luminosity bins. Given the large number of counts available we were able to further sub-divide the low luminosity bin into four bins: low1 ($\log f_{\rm X} < -11.2$), low2 ($-11.2 < \log f_{\rm X} < -11.1$), low3 ($-11.1 < \log f_{\rm X} < -11$) and low4 ($-11 < \log f_{\rm X} < -10.9$). Similarly, the high-luminosity bin was sub-divided into three bins: high1 ($-10.9 < \log f_{\rm X} < -10.8$), high2 ($-10.8 < \log f_{\rm X} < -10.75$) and high3 ($\log f_{\rm X} > -10.75$); see Fig. 2 (top panel) for the binning boundaries. We stacked the spectra in each bin together using the script ADDSPEC; the appropriate RMFs and ARFs were also combined by the script.

However, as the instrument response of the *Swift* XRT varies across the detector, combining responses with distinct differences – i.e. those of on-axis and off-axis spectra – may risk introducing uncertainties into a combined response file for the stacked spectra. To avoid this issue, we stacked the on- and off-axis spectra in each luminosity bin separately, such that we produced two spectra per bin. Finally, we grouped the stacked spectra to have a minimum of 20 counts per bin within the spectra. We note that we excluded two *Swift* observations – observation IDs 00035335004 and 00035335005 – from the following analysis since they have a high number of counts ($\gtrsim$ 2900 counts) and so would potentially dominate the stacked spectrum they are each associated with (although they also have too few counts to be analysed separately). The properties of the stacked spectra in each luminosity bin are summarized in Table 3.

We began the analysis of the stacked spectra by modelling them with the absorbed MCD plus Comptonization model. We modelled the on- and off-axis spectra of each luminosity bin simultaneously, adding a multiplicative constant to the model to allow for any calibration differences between the two spectra. The parameter was frozen at unity for the on-axis spectra, whilst that of the off-axis

[13] http://heasarc.nasa.gov/xanadu/xspec/

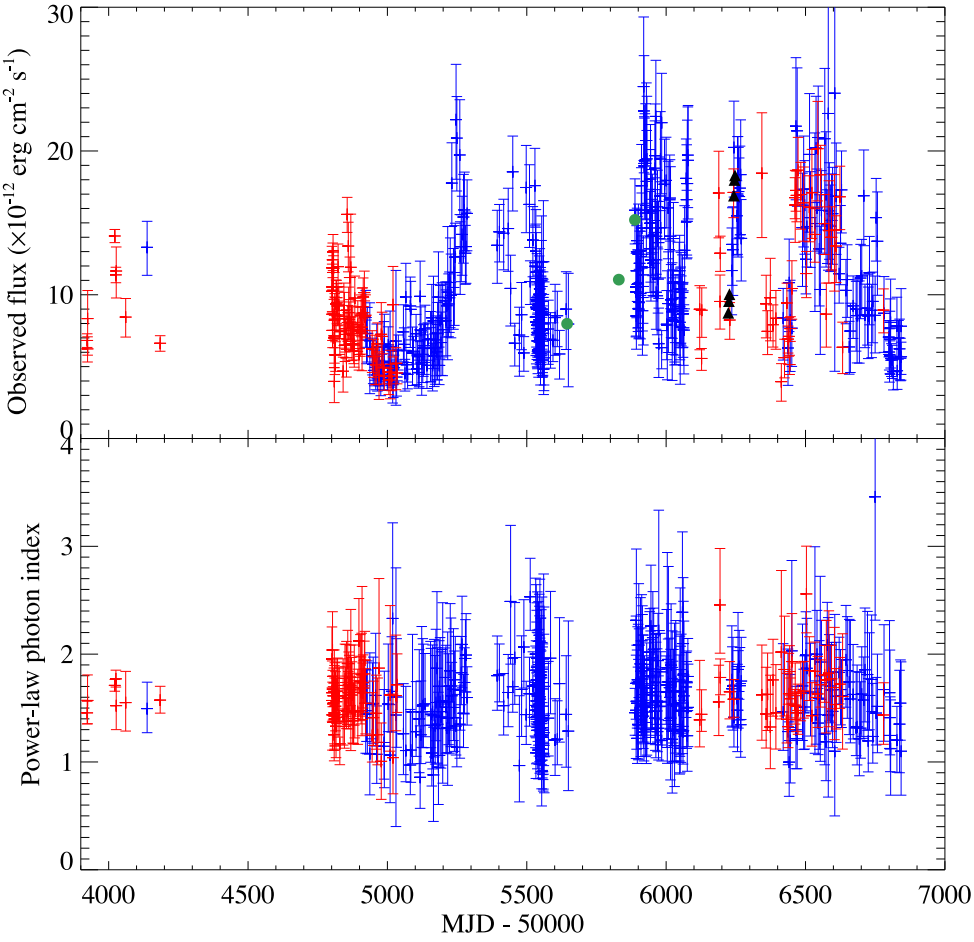

Figure 1. Top panel: the light curve of Holmberg IX X-1, obtained from *Swift* on-axis (red) and off-axis (blue) observations. The time axis runs from 2006 June to 2014 August. The solid green circles indicate the 2011 *XMM–Newton* observations, whilst the solid black triangles indicate the *XMM–Newton* observations taken contemporaneously with *NuSTAR* in 2012. Bottom panel: the photon index, plotted as a function of observing time, obtained by modelling the individual *Swift* spectra with an absorbed power-law model.

spectra was allowed to be a free parameter; we found that the disagreement between the spectra was at no more than the $\lesssim$10 per cent level.

The stacked spectra along with the best-fitting models are shown in Fig. 3. The plot reveals an interesting result; it is obvious that the spectra change shape as the luminosity increases – especially in the ∼1–6 keV energy band – from appearing as flat spectra at low luminosity to becoming more curved as the luminosity increases. This demonstrates clear evolution of the average ULX spectra with increasing luminosity. However, we found that the data were not sufficiently high quality to strongly constrain the model parameters with this choice of binning. So, in order to improve the constraints on the spectral fitting, we increased the S/N of the stacked spectra by combining those with similar characteristics in the ∼1–6 keV energy band; hence we stacked the spectra of the low1, low2 and low3 luminosity bins together as these spectra are similarly flat (hereafter the lowluminosity bin; see Table 3). In contrast, the spectra of high1, high2 and high3 luminosity bins seem to be very curved and so were stacked together (hereafter the high-luminosity bin). The spectra of the low4 luminosity bin were left to represent an intermediate spectral stage between the flat and curved spectra; hereafter we refer to it as the medium luminosity bin.

Again, we analysed the stacked spectra in the low, medium and high luminosity bins by modelling them with an MCD plus Comptonization model; this produced statistically acceptable fits in all cases (null hypothesis probability >0.05), and the best-fitting results are reported in Table 4 and shown in Fig. 4. Overall, similar spectral evolution to the previous, finer flux segregation is found; the average spectra are flat at low luminosity and become more curved at higher luminosity. They appear most curved at the highest ULX luminosity. Hence it appears that the two peaks in Fig. 2 occur where the spectra appear different; flat in the low luminosity bin, and curved in the medium and high-luminosity bins.

We can further examine the changes in the average spectra by looking at what happens to the two components in the spectral fits. At low luminosity, the spectral fit is dominated by the COMPTT component; the MCD component makes a no contribution, resulting in the flat spectrum. As the luminosity increases, the MCD component emerges to dominate the soft end of the medium and high luminosity spectra, whilst the COMPTT component dominates the hard end. However, this MCD appears very consistent between the medium and high bins, whereas the COMPTT appears to continue to change, with its peak evolving towards a lower temperature as the luminosity increases in all three spectra (although we note that the parameter values for the fits to the three data sets shown in Table 4 are formally indistinguishable at the 90 per cent level, with the exception of the higher absorption column in the low luminosity spectrum, and the MCD changing from absent to providing between roughly a third

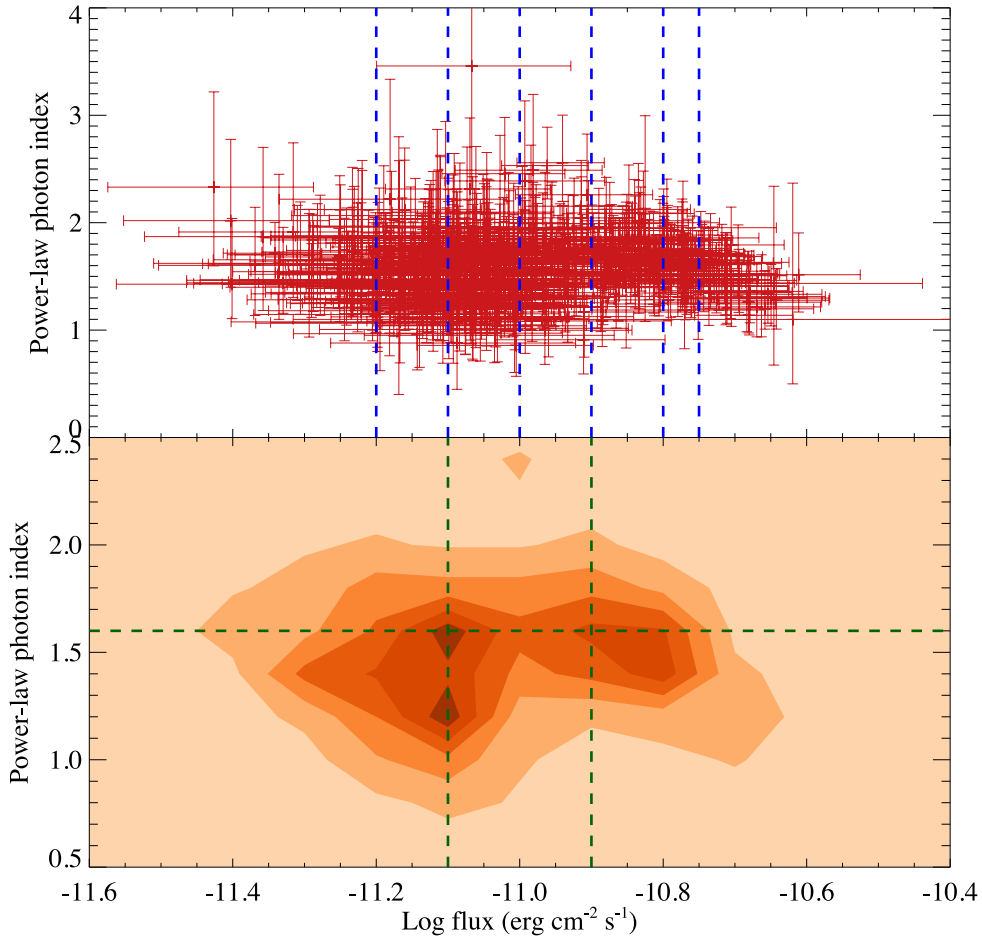

Figure 2. Top panel: the hardness-intensity diagram, obtained by fitting the individual *Swift* spectra with an absorbed power-law model. The boundaries used to segregate the *Swift* spectra into luminosity bins are plotted as blue dashed lines (see Section 3.1.2). Bottom panel: the contour plot of the data density corresponding to the plot above. The boundaries used to segregate the *Swift* spectra into the spectral index–luminosity bins are plotted as green dashed lines (see Section 3.1.3).

and a half of the flux in the high-luminosity spectrum). It is this apparent cooling of the corona, combined with the emergence of the MCD, that leads to the increasingly curved spectra at higher luminosities.

3.1.3 Stacked spectral analysis: photon index and luminosity segregation

The hardness-intensity diagram in Fig. 2 shows that the distribution of the data has definite structure. In the previous section, we examined the spectral evolution based on luminosity criteria alone. However, the hardness-intensity diagram also demonstrates that the photon indexes of individual *Swift* spectra vary widely for the same luminosity, between ∼1 and 2.5. Indeed, there is even some evidence in the bottom panel of Fig. 2 for the low luminosity density peak having two distinct sub-peaks, either side of $\sim\Gamma = 1.4$. This strongly suggests that the average spectra are not a simple function of luminosity. Thus, in this section, we re-examine the *Swift* spectra using new binning criteria that combine the observed luminosities and spectral indexes of the individual observations. First, we divided the spectra into hard ($\Gamma < 1.6$) and soft ($\Gamma > 1.6$) spectral bins. Then we further segregate the spectra in these bins into three luminosity bins: low ($\log f_X < -11.1$), medium ($-11.1 < \log f_X < -10.9$) and high ($\log f_X > -10.9$), whose boundaries are shown in the bottom panel of Fig. 2. The criteria result in six spectral bins, the properties of which are summarized in Table 3.

We stacked the spectra in each bin together using the script ADDSPEC. Again, for each spectral bin, we stacked the on- and off-axis spectra separately. We note that, in this section, we do not include the low count *Swift* spectra in the analysis (the 55 observations that have no more than between 50 and 100 counts); as these spectra have an assumed spectral index of 1.6 (see Section 3.1.1), they cannot be assimilated into either the hard or soft spectral bins. Finally, we grouped the stacked spectra to have a minimum of 20 counts per bin within each spectrum, and analysed the evolution of the spectra using the same model as in Section 3.1.2. The best-fitting results are shown in the lower panel of Table 4. We illustrate the spectral evolution with increasing luminosity, for the soft and hard bins separately, in Fig. 5.

The results obtained from this binning method are very interesting; the spectra in the hard and soft spectral bins show different evolution with increasing luminosity. For the hard spectra, the overall spectral evolution in shape is broadly consistent with that of the pure luminosity binning shown Section 3.1.2; the spectra seem to be flat in the ∼1–6 keV range at low luminosity, and to become curved at high luminosity. The detailed evolution of the two components is, however, somewhat different. The MCD component contributes at roughly the same, low level to the total spectra at low and medium

Table 3. The properties of the stacked *Swift* spectra.

Spectral bin[a]	No. of spectra[b]		Total counts[c]	
	on-axis	off-axis	on-axis	off-axis
	Luminosity binning			
Low1(Low)	23	60	4494	6374
Low2(Low)	29	58	10 069	7764
Low3(Low)	36	89	11 275	14 318
Low4(Medium)	13	45	5804	8625
High1(High)	10	51	5372	13 287
High2(High)	11	31	6587	8661
High3(High)	4	33	1574	9564
	Photon index and luminosity binning			
	Hard spectral bin			
Low	23	46	8202	6158
Medium	20	78	6372	12 152
High	11	56	7704	15 736
	Soft spectral bin			
Low	23	31	5898	4549
Medium	26	55	10 495	10 704
High	14	55	5829	15 480

Note. [a]The names of the stacked *Swift* spectral bins. Those in brackets indicate the new names after the spectra are re-binned to further improve S/N (see Section 3.1.2). [b]The number of *Swift* spectra contributing to each spectral bin. [c]The total number of photon counts from all spectra contributing to the spectral bin.

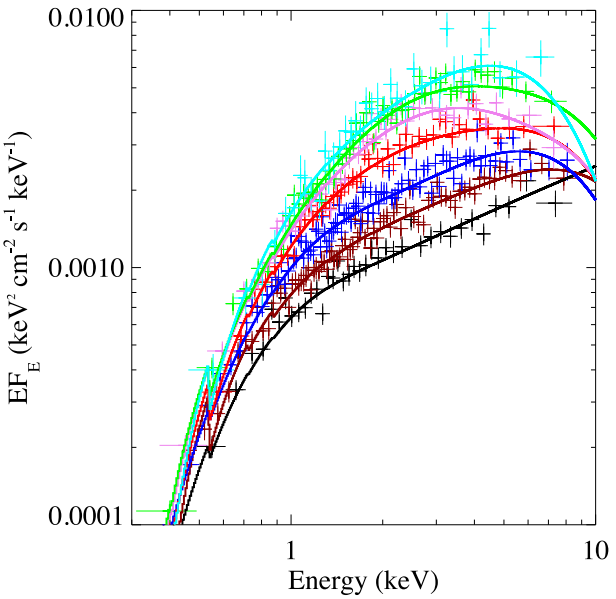

Figure 3. The stacked *Swift* spectra, showing (from bottom to top) the low1 (black), low2 (brown), low3 (blue), low4 (red), high1 (violet), high2 (green) and high3 (cyan) luminosity bins. Only on-axis spectra are shown, and they are re-binned to a minimum of 10σ statistical significance (5σ statistical significance for the high3 luminosity bin spectrum) per data point to clarify the plot. The best-fitting absorbed MCD plus COMPTT model for each spectrum is also shown by the solid lines.

luminosity (<20 per cent of the total unabsorbed flux). However, at high luminosity, the component becomes very significantly hotter (cf. Table 4) and dominates the soft end of the spectrum, contributing ∼40 per cent of the total flux (although again we cannot formally exclude the lower limit on this contribution from overlapping with the low and medium bin contributions). In contrast, the COMPTT component is very dominant at low and medium luminosity; however, at high luminosity, the component only dominates the hard band. We do, however, see the same apparent gradual decrease in temperature in the hard component as the total luminosity increases as for the pure luminosity binning, but again have the same caveat about a lack of formal distinction at the 90 per cent significance level.

In contrast, the evolution of the soft spectra with luminosity is somewhat different from that of the hard spectra, in particular at low and medium luminosity (see right-hand panel of Fig. 5). Overall, the spectrum appears to be distinctly two component in the low luminosity bin; however, as the luminosity increases, the individual components of the MCD and COMPTT seem to merge together, resulting in a single-component-like curved spectrum. Furthermore, unlike the hard spectra, the MCD component always appears to dominate the softer energy band of the spectra, contributing ∼35–50 per cent of the total unabsorbed flux, and remains roughly constant in temperature as the luminosity increases (i.e. does not evolve very dramatically with increasing total luminosity). These MCD components are distinctly different from those of the hard spectra, showing significantly higher fractional contributions to the overall flux, and temperatures, than the MCD components in the corresponding hard spectra. In the soft spectra the COMPTT component also shows possible temperature evolution, displaying the same pattern in apparent decreasing peak energy as the luminosity increases as is seen in the other analyses, although this again remains unconfirmed within the uncertainty limits on the parameter fitting.

3.2 *XMM–Newton* spectral analysis

Unlike the *Swift* spectra, the 13 *XMM–Newton* spectra were of sufficiently high quality to enable us to study Holmberg IX X-1 without stacking. We analysed these spectra using the same model as for the *Swift* stacked spectra in Sections 3.1.2 and 3.1.3. For each individual observation, we model the PN, MOS1 and MOS2 spectra simultaneously, adding a multiplicative constant to the model to correct for any residual calibration differences between the *XMM–Newton* detectors; in practise this offset is at the $\lesssim 10$ per cent level. The best-fitting results are tabulated in Table 5; to facilitate comparison with the other analyses, we sort the spectra in ascending order of their observed luminosities and also classify each *XMM–Newton* spectrum into an appropriate luminosity group, corresponding to the boundaries defined in Section 3.1.2. Acceptable fits were found in all but 2 cases; observation ID 0200980101 is very marginally rejected (null hypothesis probability of 0.04), and 0111800101 was rejected with a null hypothesis of $\sim 5 \times 10^{-3}$, i.e. an $\sim 3\sigma$ confidence rejection. However, it is notable that these observations are the highest quality data for Holmberg IX X-1 and that there is a suggestion of residuals in the soft X-ray emission, in common with other ULXs, that may be causing this result (Middleton et al. 2015b).

We show the spectral evolution of Holmberg IX X-1 with luminosity, as seen by *XMM–Newton*, in Fig. 6. Overall, we see some broad consistencies with the *Swift* stacked spectra. There are some obvious degeneracies in spectral shape with luminosity, as suggested by splitting the stacked *Swift* spectra into hard and soft bins, particularly in the low and high luminosity *XMM–Newton* groups. In the low luminosity group this manifests as both distinct two-component and flat spectral shapes (with the flat spectra apparently slightly more luminous); in the high-luminosity group the differences are mainly in the turnover of the hard component. However, we again see the same trends in the data, with mostly flatter data (in

Table 4. The best-fitting parameters for the stacked *Swift* spectra modelled by an MCD plus Comptonization model.

Spectral bin	$N_{\rm H}{}^{a}$	$kT_{\rm in}{}^{b}$ (keV)	$kT_{\rm e}{}^{c}$ (keV)	$\tau_{\rm e}{}^{d}$	χ^2/d.o.f.^{e}	$L_{\rm X}{}^{f}$	$f_{\rm MCD}/f_{\rm tot}{}^{g}$
			Luminosity binning				
Low	$0.19^{+0.03}_{-0.01}$	<0.11	$2.61^{+0.41}_{-0.28}$	$7.45^{+0.52}_{-0.59}$	1028.85/970	$10.42^{+0.14}_{-0.16}$	0.00^{h}
Medium	$0.12^{+0.02}_{-0.07}$	$0.81^{+0.41}_{-0.51}$	$1.89^{+1.04}_{-0.51}$	>7.15	441.40/482	$15.43^{+0.67}_{-0.64}$	<0.60
High	0.12 ± 0.01	$0.73^{+0.96}_{-0.15}$	$1.87^{+81.77}_{-0.30}$	>1.57	819.04/849	$20.19^{+0.48}_{-0.22}$	$0.37^{+0.12}_{-0.07}$
			Photon index and luminosity binning				
			Hard spectral bin				
Low	$0.21^{+0.09}_{-0.05}$	$0.16^{+0.04}_{-0.02}$	$2.44^{+0.84}_{-0.39}$	$8.45^{+1.24}_{-1.41}$	496.78/501	$9.19^{+0.34}_{-0.32}$	$0.13^{+0.05}_{-0.11}$
Medium	0.20 ± 0.09	$0.14^{+0.04}_{-0.03}$	$1.96^{+0.29}_{-0.20}$	$9.53^{+1.02}_{-0.98}$	614.57/580	$12.61^{+0.42}_{-0.40}$	<0.20
High	$0.11^{+0.02}_{-0.01}$	$0.82^{+0.76}_{-0.28}$	>1.03	>0.97	706.40/665	$20.47^{+0.77}_{-0.66}$	$0.40^{+0.32}_{-0.26}$
			Soft spectral bin				
Low	0.10 ± 0.02	$0.85^{+0.12}_{-0.39}$	>1.89	>3.43	312.87/391	$9.78^{+0.62}_{-0.50}$	$0.53^{+0.04}_{-0.21}$
Medium	0.13 ± 0.02	$0.78^{+0.31}_{-0.34}$	$2.24^{+3.46}_{-0.59}$	$9.56^{+67.50}_{-3.06}$	621.86/601	$13.20^{+0.51}_{-0.44}$	$0.50^{+0.09}_{-0.23}$
High	$0.13^{+0.02}_{-0.03}$	$0.68^{+0.37}_{-0.19}$	>1.23	>0.17	567.48/588	$19.88^{+0.78}_{-0.71}$	$0.34^{+0.10}_{-0.11}$

Note. [a]Absorption column external to our Galaxy, in units of 10^{22} cm^{-2}. [b]The inner disc temperature of the MCD component. [c]The plasma temperature of the Comptonizing corona. [d]The optical depth of the Comptonizing corona. [e]Minimum χ^2 over degrees of freedom. [f]Observed X-ray luminosity in the 0.3–10 keV energy band, in units of 10^{39} erg s^{-1}. [g]The ratio of MCD flux to total unabsorbed X-ray flux in the 0.3–10 keV energy band. [h]No flux contribution from the MCD component in the best-fitting model to this data set.

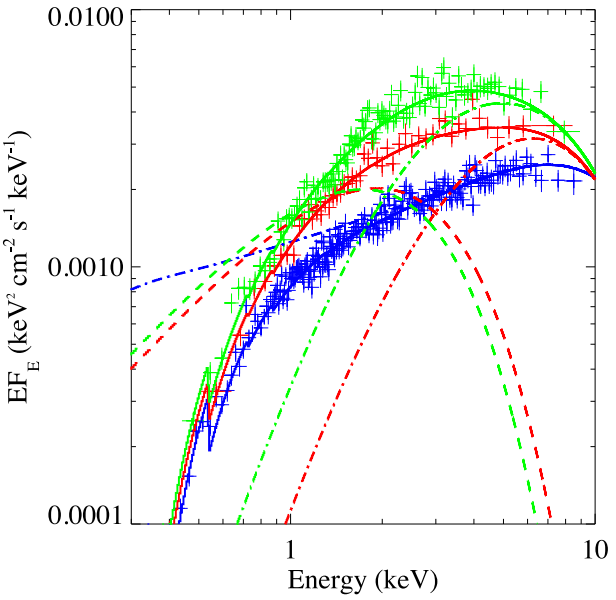

Figure 4. The stacked *Swift* spectra in (from bottom to top) the low (blue), medium (red) and high (green) luminosity bins. Only on-axis spectra are shown and they are re-binned to a minimum of 10σ statistical significance for clarity. The best-fitting absorbed MCD plus COMPTT models are shown as solid lines; the individual components, corrected for absorption, are also plotted as the dashed (MCD) and dash–dotted lines (Comptonization).

the 1–6 keV range) giving way to much more pronounced curvature as the luminosity of Holmberg IX X-1 increases.

The evolution of the two individual components is also interesting. In the low and medium luminosity groups, only a small fraction of the total spectrum originates in the MCD component (generally <20 per cent), and its properties remain approximately constant (e.g. $kT_{\rm in}$ is invariant within errors; see Table 5) as the luminosity increases from low to medium luminosity. However, in the high-luminosity group, this component contributes significantly more to the spectrum in 3/5 cases (∼40 per cent of the total unabsorbed flux), and in these cases is significantly warmer (∼0.7 keV as opposed to ∼0.25 keV); however there remain two cases – observation ID 0657802201 and 0693851801 – in which the MCD temperatures and contributions are as low as those of the low luminosity bin. The COMPTT dominates the spectra in the low and medium luminosity groups, and remains dominant at the hard end of the spectrum in the high-luminosity group. However, its temperature is demonstrably cooler as the luminosity increases, with $kT_{\rm e} > 2$ keV in the low and medium luminosity groups, but $kT_{\rm e} < 2$ keV in the high-luminosity group (significant at the >90 per cent level in most cases), consistent with the trend noted qualitatively for the stacked *Swift* spectra.

3.3 Broad-band spectral analysis

We have shown that the spectral evolution in the 0.3–10 keV range observed by *Swift* and *XMM–Newton* appears to follow a set pattern, albeit with some level of spectral degeneracy with luminosity. However, with *NuSTAR* we now have data that extends our bandpass for observing ULXs above 10 keV (e.g. Bachetti et al. 2013; Walton et al. 2013b). Therefore, in this section we extend our analysis to the 0.3–30 keV range[14] using two epochs of *XMM–Newton* and *NuSTAR* data taken contemporaneously in 2012 (see Sections 2.2 and 2.3; also Walton et al. 2014). We model the *XMM–Newton* and *NuSTAR* spectra from each epoch together, adding a constant multiplicative factor into the model to correct for any calibration differences between all *XMM–Newton* and *NuSTAR* detectors; a $\lesssim$ 10 per cent difference in the constant parameter is required. We began by modelling the broad-band spectra using the same MCD plus COMPTT model used successfully for the stacked *Swift* and the *XMM–Newton* spectra. However, the data reject the model for both epochs of spectral data (null hypothesis probability $\lesssim 0.01$; see Table 6).

[14] The *NuSTAR* observing bandpass extends to ∼79 keV, however no significant detection of Holmberg IX X-1 is made above 30 keV (Walton et al. 2014).

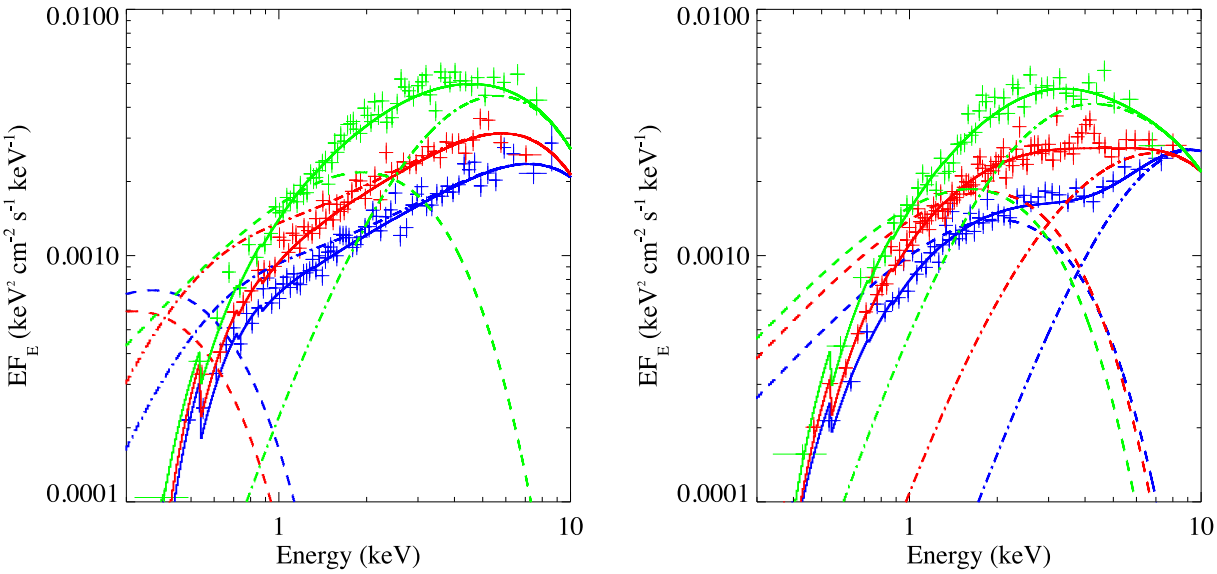

Figure 5. The stacked *Swift* spectra binned by a combination of spectral index and luminosity criteria. Left-hand panel: the stacked hard spectra. Right-hand panel: the stacked soft spectra. Only on-axis spectra are shown and they are re-binned to a minimum of 10σ statistical significance per data point to clarify the plot. The line styles, colours and order of the spectra are as per Fig. 4.

Table 5. The best-fitting results for the *XMM–Newton* spectra modelled by an MCD plus Comptonization model.

Obs. ID	$N_H{}^a$	$kT_{in}{}^b$ (keV)	$kT_e{}^c$ (keV)	$\tau_e{}^d$	χ^2/d.o.f.^{e}	$L_X{}^f$	$f_{MCD}/f_{tot}{}^g$	Group^h
0200980101	0.11 ± 0.01	0.26 ± 0.02	$2.25^{+0.15}_{-0.13}$	$9.63^{+0.61}_{-0.54}$	(536.48/482)	8.50 ± 0.09	0.19 ± 0.01	Low
0112521001	0.11 ± 0.02	0.25 ± 0.05	$2.57^{+0.94}_{-0.45}$	$7.54^{+1.39}_{-1.40}$	324.22/336	9.83 ± 0.24	$0.16^{+0.03}_{-0.05}$	Low
0657802001	$0.16^{+0.05}_{-0.04}$	$0.24^{+0.05}_{-0.04}$	>2.41	$0.75^{+38.69}_{-0.61}$	200.62/205	$11.17^{+0.48}_{-0.47}$	$0.19^{+0.03}_{-0.04}$	Low
0112521101	$0.10^{+0.03}_{-0.06}$	$0.22^{+0.06}_{-0.04}$	$2.64^{+0.72}_{-0.42}$	$6.95^{+1.04}_{-0.95}$	368.12/350	11.27 ± 0.23	<0.17	Low
0693850801	$0.10^{+0.03}_{-0.06}$	0.22 ± 0.04	>3.15	$1.07^{+4.88}_{-1.02}$	382.71/347	12.24 ± 0.25	<0.11	Low
0693850901	$0.11^{+0.03}_{-0.07}$	$0.26^{+0.10}_{-0.07}$	$2.46^{+0.67}_{-0.45}$	$7.61^{+1.86}_{-1.26}$	362.56/364	13.38 ± 0.31	<0.18	Low
0693851001	$0.10^{+0.02}_{-0.06}$	$0.30^{+0.20}_{-0.08}$	$2.16^{+0.52}_{-0.46}$	$8.27^{+4.61}_{-1.35}$	328.58/329	$14.05^{+0.34}_{-0.33}$	$0.17^{+0.07}_{-0.16}$	Medium
0657801801	$0.08^{+0.03}_{-0.07}$	$0.28^{+0.11}_{-0.04}$	$2.56^{+0.98}_{-0.43}$	$6.89^{+1.17}_{-1.23}$	331.12/354	$15.47^{+0.41}_{-0.40}$	<0.24	Medium
0111800101	0.13 ± 0.01	$0.52^{+0.33}_{-0.18}$	$1.30^{+0.09}_{-0.11}$	>11.39	(363.79/297)	$19.20^{+0.32}_{-0.31}$	$0.36^{+0.10}_{-0.13}$	High
0657802201	$0.10^{+0.03}_{-0.04}$	$0.28^{+0.07}_{-0.03}$	$1.97^{+0.16}_{-0.13}$	$8.38^{+0.61}_{-0.48}$	391.12/415	$21.28^{+0.32}_{-0.31}$	$0.09^{+0.04}_{-0.06}$	High
0693851701	$0.11^{+0.01}_{-0.02}$	0.71 ± 0.17	$1.76^{+0.17}_{-0.13}$	$11.77^{+3.83}_{-1.68}$	432.58/406	$23.65^{+0.34}_{-0.35}$	<0.47	High
0693851801	$0.07^{+0.04}_{-0.06}$	$0.26^{+0.07}_{-0.03}$	$1.54^{+0.06}_{-0.05}$	$11.43^{+0.47}_{-0.41}$	428.36/407	25.17 ± 0.33	<0.12	High
0693851101	0.11 ± 0.02	$0.77^{+0.41}_{-0.24}$	$1.92^{+0.38}_{-0.22}$	>8.57	384.06/355	25.62 ± 0.55	$0.44^{+0.10}_{-0.11}$	High

Note. [a]Absorption column external to our Galaxy, in units of 10^{22} cm^{-2}. [b]The inner disc temperature of the MCD component. [c]The plasma temperature of the Comptonizing corona. [d]The optical depth of the Comptonizing component. [e]Minimum χ^2 over degrees of freedom. Parentheses highlight fits for which the null hypothesis probability is <0.05. [f]Observed X-ray luminosity in the 0.3–10 keV energy band, in units of 10^{39} erg s^{-1}. [g]The ratio of MCD flux to the total unabsorbed X-ray flux in the 0.3–10 keV energy band. [h]The luminosity bin of the *XMM–Newton* spectra. We classify the spectra using the same luminosity boundaries used to create the *Swift* low, medium and high luminosity spectra in Section 3.1.2.

It is no surprise that a simple MCD plus COMPTT model does not give a good fit, given that this has been demonstrated in several *NuSTAR* papers on different ULXs (e.g. Bachetti et al. 2013; Walton et al. 2014 etc.). In these papers it is demonstrated that an additional hard component may be present in the data above 10 keV. We have attempted to account for the hard excess in the data by adding an additional component into the model, a SIMPL model that is an empirical approximation of Comptonization in which an input seed spectrum is scattered into a power-law component (Steiner et al. 2009). In this we directly follow the models used in Walton et al. (2014), who model the same broad-band data set and propose two different spectral evolution scenarios. These are based on two models: DISKBB+SIMPL×DISKPBB and DISKBB+SIMPL×COMPTT. In the first case the hard component is modelled by an approximation for an advection-dominated 'slim' accretion disc in which the temperature profile of the disc is modelled as $T(r) \propto r^{-p}$ and values of $p \approx 0.5$ indicate a slim disc (e.g. Vierdayanti et al. 2006 and references therein); in the second it is modelled by the same COMPTT we have been using previously.

Both models fit equally well to the data and the spectral evolution of the models with luminosity is similar to that is described in Walton et al. (2014). In brief, the evolution obtained from DISKBB+SIMPL×DISKPBB suggests that evolution is mainly in the MCD component, that increases dramatically in both

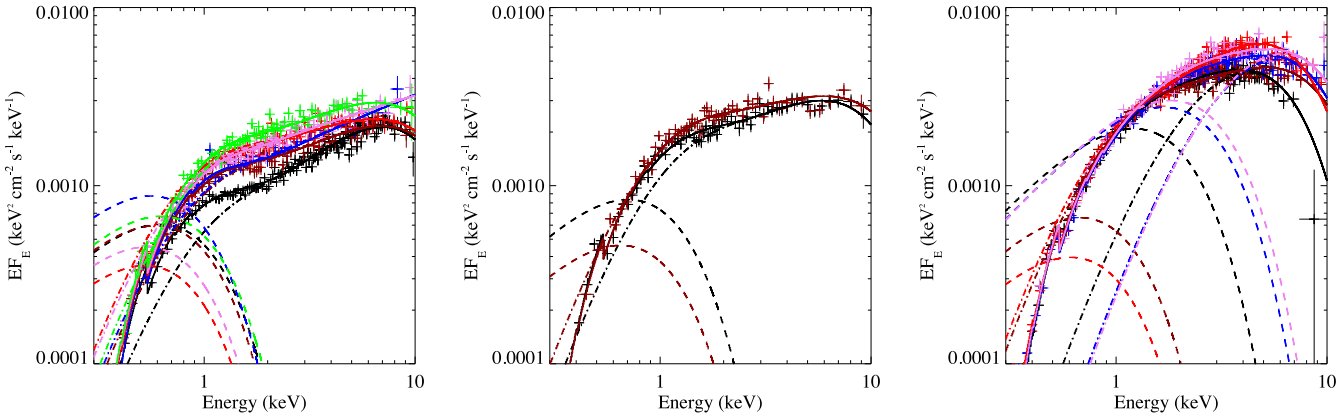

Figure 6. The *XMM–Newton* spectra, segregated into low (left-hand panel), medium (middle panel) and high (right-hand panel) luminosity groups using the same luminosity boundaries used to create the stacked *Swift* spectra. Only PN spectra (or MOS1 in case of ObsID. 0111800101) are shown and they are re-binned to a minimum of 10σ statistical significance for clarity. The best-fitting absorbed MCD plus COMPTT model is also shown as solid lines; the individual components of MCD and Comptonization, corrected for absorption, are also plotted as dashed lines and dash–dotted lines, respectively. For each panel, the colour coding is used to indicate the relative luminosity of the source, ascending in order of increasing luminosity from black to brown, blue, red, violet and green.

Table 6. The results of joint *XMM–Newton* and *NuSTAR* spectral fits.

Model	N_H[a]	kT_{in}[b] (keV)	kT_0 or Γ[c]	per cent$_{scat}$[d]	kT_2[e] (keV)	τ or p[f]	χ^2/d.o.f.[g]
Epoch 1: low/medium luminosity ($f_X = 1.08 \times 10^{-11}$ erg cm^{-2} s^{-1})[h]							
DISKBB+COMPTT	$0.22^{+0.04}_{-0.02}$	$0.09^{+0.02}_{-0.04}$	–	–	3.22 ± 0.09	6.02 ± 0.16	(1625.53/1499)
DISKBB+(SIMPL×COMPTT)	0.14 ± 0.02	$0.29^{+0.06}_{-0.02}$	$3.80^{+0.31}_{-0.10}$	>70	$2.08^{+0.08}_{-0.12}$	7.47 ± 0.26	1558.54/1497
DISKBB+(SIMPL×DISKPBB)	$0.16^{+0.02}_{-0.03}$	$0.27^{+0.08}_{-0.06}$	$3.28^{+1.38}_{-1.35}$	27^{+47}_{-22}	$3.46^{+0.35}_{-0.42}$	$0.56^{+0.01}_{-0.01}$	1557.04/1497
Epoch 2: high luminosity ($f_X = 1.72 \times 10^{-11}$ erg cm^{-2} s^{-1})[h]							
DISKBB+COMPTT	0.08 ± 0.004	$1.20^{+0.07}_{-0.06}$	–	–	$2.85^{+0.12}_{-0.11}$	$6.61^{+0.75}_{-0.53}$	(2082.89/1815)
DISKBB+(SIMPL×COMPTT)[i]	$0.15^{+0.02}_{-0.01}$	$0.32^{+0.07}_{-0.04}$	$3.59^{+0.08}_{-0.02}$	>85	$1.06^{+0.02}_{-0.04}$	$11.67^{+0.06}_{-0.61}$	1869.45/1813
DISKBB+(SIMPL×COMPTT)[j]	0.12 ± 0.003	0.58[k]	$3.56^{+0.08}_{-0.02}$	>81	$1.01^{+0.01}_{-0.04}$	$11.92^{+0.08}_{-0.02}$	1886.80/1813
DISKBB+(SIMPL×DISKPBB)	$0.14^{+0.02}_{-0.01}$	1.63 ± 0.06	>3.16	60^{+7}_{-39}	$3.19^{+0.72}_{-0.17}$	0.55 ± 0.01	1873.24/1813

Note. [a]Absorption column beyond our Galaxy, in units of 10^{22} cm^{-2}. [b]The inner disc temperature of the MCD component. [c]The seed photon temperature of the COMPTT component (in units of keV) or the power-law photon index of the SIMPL component. [d]The scattered fraction of the SIMPL component. [e]The plasma temperature of the COMPTT component or the inner disc temperature of the DISKPBB component. [f]The optical depth of the COMPTT component or the value of the p parameter in the DISKPBB component. [g]Minimum χ^2 over degrees of freedom from the fit. [h]Observed X-ray flux in the 0.3–10 keV energy band calculated from the DISKBB+(SIMPL×COMPTT) model. [i]The best-fitting result obtained from the global minimum χ^2 statistic. [j]The fitting result obtained from the local minimum statistic (see text). [k]We were unable to place constraints on this parameter.

temperature (from ∼0.3 to ∼1.6 keV) and flux (∼4 to ∼44 per cent of the total unabsorbed flux) in the high-luminosity epoch, whilst the DISKPBB component appears much closer to constant between the two epochs (see the left-hand panel of Fig. 7). In contrast, the evolution obtained from DISKBB+SIMPL×COMPTT appears in the opposite sense. The MCD component seems to remain constant whilst the COMPTT component appears to play a much larger role in the evolution of the spectra when the luminosity increases (although in both cases very high scattered fractions for the SIMPL component are required, >70 per cent), as is shown in the right-hand panel of Fig. 7. However, we note that the spectral evolution obtained from the DISKBB+SIMPL×COMPTT model may not be unique; in fact, we found a local minimum in the χ^2 fitting of epoch 2 spectra where the $\Delta\chi^2$ between the global and local minimum is only ∼20 over 1813 degrees of freedom, so we cannot reject the result obtained from this minimum. Interestingly, the spectral evolution suggested by the local minimum is more consistent with the evolution obtained from the MCD plus COMPTT model, particularly for the *Swift* and *XMM–Newton* data, in which the MCD component gets stronger and warmer, and the COMPTT component peaks at lower energy when the luminosity increases. We will discuss this further in Section 4.

4 DISCUSSION

Holmberg IX X-1 is a persistently luminous ULX, with a decade of monitoring by *Swift* showing a dynamical range of a factor of $\lesssim 5$ and a typical luminosity of around $\sim 10^{40}$erg s^{-1}. In this paper we have examined the spectral evolution of this ULX with changes in luminosity, based on stacking *Swift* spectra in terms of their flux and as a combination of their flux and photon index (with the latter as a proxy for X-ray colour), on *XMM–Newton* pointed observations, and on combining contemporaneous *XMM–Newton* and *NuSTAR* data to provide a broader bandpass in which to study the variation of the ULX. Our main finding is that there appears to be a common trend in the changing morphology of the spectrum as the luminosity increases, albeit with evidence for some level of degeneracy with luminosity. At lower luminosities (around 10^{40}erg s^{-1}) we see the spectra as either a distinct, two-component ULX spectrum with a

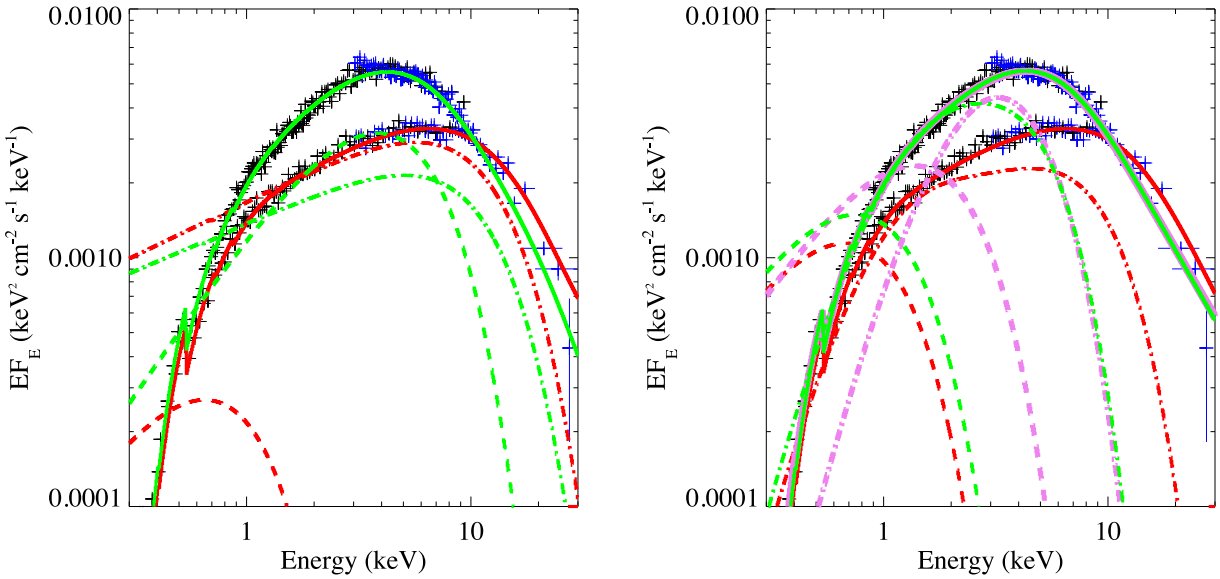

Figure 7. The DISKBB+SIMPL×DISKPBB model (left-hand panel) and DISKBB+SIMPL×COMPTT model (right-hand panel), fitted to the broad-band spectra of Holmberg IX X-1 observed by *XMM–Newton* (black) and *NuSTAR* (blue). The best-fitting models are plotted as solid lines for both epoch 1 (red, lower flux) and epoch 2 (green) spectra. The MCD components, corrected for absorption, are plotted as dashed lines, whilst the DISKPBB or COMPTT components, corrected for absorption and modified by the SIMPL model, are plotted as the dash–dotted lines. The violet lines in the right-hand panel are the fitting result for epoch 2 spectra obtained from the local model minimum (see text).

dominant hard component, or as a hard, flat spectrum in the 1–6 keV range, with a turnover in the spectrum at higher energies. These spectra would classify Holmberg IX X-1 as in the *HUL* regime of Sutton et al. (2013). However, as the luminosity increases to $\sim 2 \times 10^{40}$ erg s^{-1}, its shape changes to become much more curved and disc-like, with a single peak at energies of $\sim$ 4–5 keV (indeed, it is likely that some of these spectra would be classified as *broadened disc* according to the Sutton et al. 2013 scheme).

The spectra in the 0.3–10 keV bandpass of *Swift* and *XMM–Newton* are all satisfactorily described by a model composed of two thermal components, a multicolour disc blackbody model for the soft end of the spectrum, and an optically thick, cool Comptonizing corona for the hard end, with the seed photon temperature of the latter fixed at the temperature of the disc. Such a model has been found to be a good empirical description of ULX spectra in this bandpass, albeit with strong caveats against the direct physical interpretation of this model (e.g. Gladstone et al. 2009), and allows us to track the variation of the two components that make up the model. However, when the spectral bandpass is extended above 10 keV by the use of *NuSTAR* data, we find that this model no longer constitutes an acceptable fit to the data, as has been found for multiple *NuSTAR* observations of ULXs where additional hard flux is required (although this is somewhat model dependent in several ULXs; Walton et al. 2015 and references therein). Here, we accounted for the extra hard flux using an additional component, the SIMPL model. Two models – DISKBB+SIMPL×DISKPBB and DISKBB+SIMPL×COMPTT – were used to fit the data, and they were found to equally well describe the broad-band spectra.

4.1 The model-dependent variability of individual spectral components

In this work, we primarily used an MCD plus Comptonization model to analyse the ULX spectra. Although this model has strong caveats about its direct physical interpretation (see above), tracking the variability of each individual spectral component might provide some useful information about the change in the properties and/or geometry of the accretion disc. We found that the behaviour of the individual MCD and COMPTT components appear to follow general patterns in the 0.3–10 keV data, although this is somewhat confused by the degenerate behaviours. In most of the *Swift* and *XMM–Newton* data the variability is mainly in the Comptonized component, that brightens but appears to drop to a lower peak energy (i.e. cools down) as the total luminosity increases. The MCD component is mostly relatively stable, although it does appear to brighten and warm up in the most luminous data sets. However, the behaviour becomes much less certain when the *NuSTAR* data are included. Here, we tried multiple models in common with other work, and found that the variability of individual components seems to be dependent on the model used to fit the spectra. In the modified version of the MCD plus Comtonization model, with an additional SIMPL component to represent the required hard excess, the evolution is uncertain, with the COMPTT cooling but fits with the MCD both remaining the same, and increasing in temperature and flux, are permitted. The situation is confused further by the use of a DISKPBB 'slim disc' model in place of the COMPTT, in which case the variability is dominated by the MCD and the slim disc remains relatively stable between the two epochs. Thus, the real evolution of the soft and hard components appears highly uncertain, with the evolution we see depending upon the models we use to fit the data.

If this is the case when we fit the broad-band data, then this raises real questions over the fits in the more limited 0.3–10 keV band. Specifically, is the behaviour of the two components similarly model-dependent in this band? We investigate this by re-modelling the *Swift* luminosity bin spectra using two alternative simple, empirical models (with, particularly in the latter case, no direct physical interpretation for a ULX) that have been shown to fit ULX data in this band (Stobbart et al. 2006), namely a blackbody plus MCD model (BB + DISKBB in XSPEC) and a double MCD component model (DISKBB + DISKBB in XSPEC). The fitting results show that both

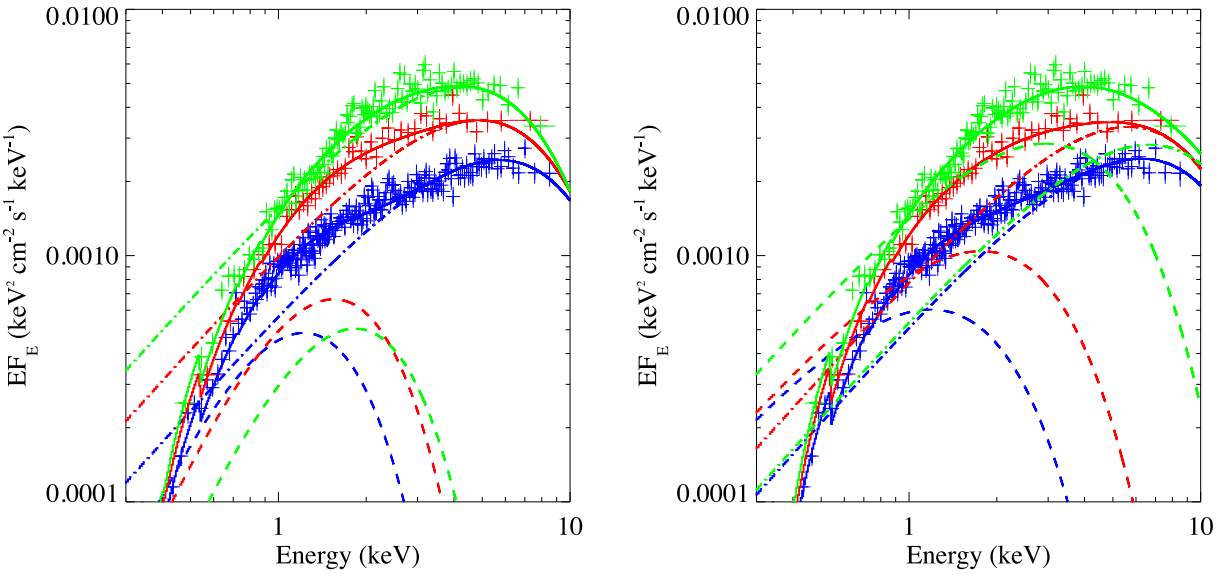

Figure 8. The *Swift* luminosity bin spectra fitted by the BB + DISKBB model (left-hand panel) and DISKBB + DISKBB model (right-hand panel). Only on-axis spectra are shown and they are re-binned to a minimum of 10σ statistical significance per data point to clarify the plot. The line styles, colours and order of the spectra are as per Fig. 4, excepting for the dashed lines and the dash–dotted lines which here represent the lower energy components (BB for the left-hand panel and lower temperature DISKBB for the right-hand panel) and higher energy components (DISKBB for the left-hand panel and higher temperature DISKBB for the right-hand panel), respectively.

models can adequately describe the spectra, with fits that are nearly or equally as good as the DISKBB + COMPTT model in Section 3.1.2 (the blackbody plus MCD fit is generally worse by $\Delta\chi^2$ of ∼30 for the *XMM–Newton* spectra, but still statistically acceptable). We show these fits, and their underlying component variability, in Fig. 8. Comparing the variability of the individual components seen in these two models with that in the MCD plus Comptonization model (cf. Fig. 4), we see clear differences. Whilst the variability of the high-energy component seems to follow a similar pattern across all three models – lowering in peak energy as the total luminosity increases – the low-energy components exhibit very different behaviours, in terms of both their flux and temperature. In the new models, the blackbody appears relatively stable and contributes little to the spectrum, whereas in the dual MCD model the cooler MCD brightens and heats up substantially as the ULX luminosity increases. Both these behaviours for the soft component are distinct from that seen in the MCD plus COMPTT model. Thus, the behaviour of the two components in the narrower 0.3–10 keV range also appears highly model dependent.

Independent of the spectral fits, an examination of the data shows that a remarkable feature of all the spectra is that *the data appear to show relatively little dynamical range in flux below 1 keV*, particularly compared to the 1–6 keV regime. In fact, if we examine the range in spectral normalization at both 0.5 and 3 keV in Figs 4 and 6, we see that the 0.5 keV normalization varies by factors of 1.8–2 in the two figures, compared to a variation of 4–4.3 times at 3 keV. Hence the variation in relative normalization is a factor of 2–2.5 smaller at the lower energy. This relative lack of variability in the lower energy range is strongly suggestive that any soft component in the spectrum is not varying strongly. Therefore, we can infer that the strong changes we do see in the modelled soft component may primarily be driven by the changes in the 1–6 keV band, with a hotter and brighter MCD required to help model the strongly curved spectrum seen at the highest luminosities. We therefore strongly suspect that some of the changes in the parametrization of the two-component models may be due to the limitations of the models in describing the changing shape of the spectrum, rather than representative of real underlying physical changes. Hence, we limit the remainder of our discussion to the implications of the change in the overall shape of the spectrum with luminosity for the underlying source physics, and do not discuss the two separate spectral components hereafter, except for one final point.

The behaviour of the soft component in ULX spectra has been a point of controversy, with various studies claiming that its temperature increases with source luminosity, as would be expected for an accretion disc (e.g. Miller et al. 2004, 2013), and others claiming that it decreases with luminosity, as would be expected for an optically thick outflow (e.g. Kajava & Poutanen 2009). We note here that our analysis clearly shows that some models require the soft component to heat up and brighten, similar to the expected behaviour of a disc; others show little change. However, the implication of the above discussion (particularly the relatively low dynamical range of the flux changes below 1 keV) is that this heating and brightening (where seen) is potentially an artefact of using an incorrect model on the data; it appears that it is the overall change in the spectral shape from a flat/two-component spectrum to a narrower, disc-like spectrum in the 1–6 keV range that is driving the soft component to appear to brighten and heat up. So, in this ULX at least (that we note featured in previous samples suggesting disc-like behaviour for the soft component), we do not think that the evidence for the soft component behaving like a true accretion disc is reliable.

For the remainder of the discussion we will focus on what the overall shape of the spectrum, and its variation, mean for the physics of this ULX. We will start by discussing what the implications of our results are for the two models discussed as viable possibilities for Holmberg IX X-1 by Walton et al. (2014), namely a slim accretion disc, and a wind-dominated model.

4.2 Slim accretion disc model

We first consider whether we could be observing the emission of an accretion disc. In a standard accretion disc we would expect to

see that the peak temperature of the inner disc would scale with luminosity as $L \propto T^4$, with any changes being directly attributable to changes in the mass accretion rate. However, in Holmberg IX X-1 we see the peak in the spectrum, that is characteristic of the temperature of an optically thick medium, decrease in energy as the luminosity increases. Interestingly, this could be consistent with the emission from a slim disc. At supercritical accretion rates we expect the disc to become geometrically thick as its interior becomes supported by radiation pressure from material advecting directly into the BH (e.g. Poutanen et al. 2007). This means that in sources at high inclination angles, a slim disc can become self-obscuring and so if its scaleheight increases with luminosity it will appear to get softer as more of its harder central regions become self-obscured (Vierdayanti et al. 2013).

However, there are problems with this scenario for Holmberg IX X-1. First, the indications from both its optical spectra (lack of strong radial velocity variability in its broad emission lines; Roberts et al. 2011) and its X-ray behaviour (diagnosis as in the HUL regime; Sutton et al. 2013) are that it is viewed close to face-on, and not at a high inclination angle, so self-obscuration by the disc may be difficult to achieve in this object. Secondly, if the mass accretion rate is varying, then we would expect to see this reflected in variations of the soft part of the X-ray spectrum, as this part of the disc should remain visible, with a rising mass accretion rate leading to a rise in the soft X-ray flux that is particularly pronounced below 1 keV (see e.g. fig. 1 of Vierdayanti et al. 2013). However, as noted above, the variations below 1 keV in the data we analyse are not particularly strong between different spectra, and less than those above 1 keV. Thus we do not regard this model as a particularly strong candidate for explaining the evolution of spectra with luminosity we see in this ULX.

4.3 The effect of a massive outflowing wind

It has been proposed that the soft component seen in the spectra of ULXs can be directly attributed to the presence of an optically thick, massive outflowing wind (e.g. Kajava & Poutanen 2009). Theoretically, such an outflowing wind should be launched from the disc at supercritical accretion rates (Poutanen et al. 2007; Ohsuga & Mineshige 2011; Takeuchi et al. 2013). To explain the spectral variability in the context of an outflowing wind, we consider a spectral-timing model in the supercritical regime as recently described by Middleton et al. (2015a). In this, as the accretion disc enters the supercritical regime its scaleheight H/R (where H is the height of the disc above its central plane at a radius R) increases such that $H/R \sim 1$, similarly to the slim disc model (i.e. the disc becomes geometrically thick). However, in this model the intense radiation release from the disc drives its own loosely bound outer layers away, in the form of a massive, radiatively driven wind, such that the accretion is always locally Eddington-limited. The disc and wind bound a funnel-shaped, low-density region along the rotational axis of the BH, into which the hard radiation of the inner disc can radiate freely, and/or is scattered along by the inner parts of the wind. The wind itself is an optically thick medium that emits thermally in soft X-rays. This geometry is summarized in fig. 1 of Middleton et al. (2015a, see also fig. 2 of Poutanen et al. 2007), and it is inevitable that in this geometry the observed X-ray spectrum is primarily dependent upon viewing angle. It is also dependent upon accretion rate, as the opening angle of the funnel is predicted to close as the accretion rate increases, thus driving a more massive wind (King 2009). This should mean, for a fixed line of sight, as the accretion rate increases the changes in spectrum should be predictable (cf. Middleton et al. 2015a): if viewed close to face-on, and the wind remains out of the line of sight, the spectrum should get harder as more of the hard flux is scattered over a smaller solid angle, up the line of sight towards the observer. If, however, the wind enters the line of sight then the spectrum should soften as the wind scatters some fraction of the hard photons out of the line of sight. In both cases the soft X-ray emission from the wind should increase, as the total outflow rate of the wind is proportional to the mass accretion rate (Poutanen et al. 2007).

Critically, this model provides an explanation for the comparative lack of soft variability in Holberg IX X-1. King (2009) notes that the beaming factor b (i.e. the fraction of the sky that the funnel is open to) is related to the observed luminosity as $L \propto b^{-1}$, and is related to the mass accretion rate $\dot{m}$ as $b \propto \dot{m}^{-2}$. Thus, for the hard emission emanating from the central regions of the disc, we should see its luminosity increase as $L \propto \dot{m}^2$ if we are viewing down the funnel, which is faster than the luminosity of the isotropic wind emission increases ($\propto \dot{m}$). This relative hardening of the spectra is also discussed by Middleton et al. (2015, e.g. their equation 10), and can both qualitatively and quantitatively explain how our spectra appear to vary more above 1 keV than below, including the dynamic ranges (factor $\sim$2 difference between the faintest and brightest normalizations at 0.5 keV, compared to $\sim$4 at 3 keV). Indeed, given that the luminosity of Holmberg IX X-1 is dominated by its hard X-ray emission, its dynamic luminosity range of $\sim$4 in the reported observations implies that the underlying accretion rate probably varies by a factor of $\sim$2 over the course of the decade of observations, making it a remarkably stable accretor.

If we are viewing the central regions of the critical accretion flow down the funnel, the evolution of the peak in the spectrum we see from Holmberg IX X-1 still requires an explanation. As the luminosity increases, this peak falls to lower energies. Interestingly, this spectral evolution is consistent with simulations of the Comptonized spectra of BHs at extreme supercritical accretion rates as described by Kawashima et al. (2012). They predict that at lower super-Eddington mass accretion rates, the spectra are harder than expected from a pure slim disc spectrum due to photon up-scattering in the shock-heated region near the BH (a mechanism that we note may provide an explanation for the hard excess seen in *NuSTAR* spectra). However, at higher, extreme supercritical accretion rates, the simulated spectra are softer and become curved and disc-like as the outflow funnel opening angle becomes smaller, so decreasing the number of photons that escape without entering the cool dense outflow (the wind) and being Compton down-scattered.

Thus we suggest that as the majority of hard photons we observe are scattered up the funnel, they lose some fraction of their energy in this scattering process and so the hard spectral component becomes Compton down-scattered. As the effect of this process will increase in magnitude as the funnel narrows and so a higher fraction of photons become down-scattered, this naturally explains the lower peak temperatures of the hard component as the luminosity of Holmberg IX X-1 increases.

4.4 Source precession

One feature of the spectra remains to be explained: the spectral degeneracy with luminosity. This has also previously been reported for this ULX by Vierdayanti et al. (2010), and differences in spectral shape at similar luminosities have also been reported for two other ULXs, IC 342 X-1(Marlowe et al. 2014) and Ho II X-1 (Grisé et al. 2010). These studies agree that the degeneracy demonstrates that the observed spectra of ULXs are not a function of accretion rate

alone; Vierdayanti et al. (2010) suggest that changes in the structure of the outflowing wind may be culpable for the changes in spectral shape, whereas Marlowe et al. (2014) suggest changes in accretion state (possibly between broadened disc and HUL regimes in the case of IC 342 X-1). It is also clear that this degeneracy is not a simple prediction of the wind model – assuming a fixed line of sight, the spectrum will change as described above according to the mass accretion rate, and so we do not expect any strong degeneracy in spectral shape with luminosity except perhaps when the wind comes into the line of sight and starts to diminish the hard flux. This should, however, only occur above a certain flux threshold, and not at all observed luminosities. Hence we need a further means of creating the degeneracy; and here we explore one, that the BH rotation axis of Holmberg IX X-1 precesses with respect to our line of sight, and in doing so induces the degeneracy.

Precession is a known phenomenon of Galactic BHBs, most particularly in the case of SS433 (see Fabrika 2004 for a review). This is a very apposite example for Holmberg IX X-1 as SS433 has been suggested as a hyper-Eddington accretor that would appear as a ULX if viewed face-on. The spectral variability we would expect from precession can be inferred from Kawashima et al. (2012) and Middleton et al. (2015a). Essentially, for a fixed accretion rate, we would expect the spectra to be harder when the line of sight is closer to the axis, and softer when further away. This is again due to the effect of the funnel around the BH rotation axis; closer to on-axis more hard photons from the inner disc are scattered towards the observer, whereas further from axis the edge of the funnel is reached and material in the wind starts to enter the line of sight, which both scatters away hard photons (again up the funnel) and Compton down-scatters other hard photons that pass through the lower density regions of the clumpy wind. Hence, for a fixed accretion rate, we would expect to see a constant soft component, but a hard component that diminishes and softens as the source precesses away from the BH rotation axis. It is quite plausible that this can explain the differences between the soft and hard spectra we see in Fig. 5. For example, the peak energy in all the soft spectra is lower than in the hard spectra, consistent with down-scattering in the wind. Additionally, the soft spectra also appear brighter below 2 keV than the equivalent hard spectra; this implies that their accretion rates are likely to be higher, but that hard flux is being lost to scattering in the wind. A further illustration of this effect is the differences in the MCD component in the different observations in the *XMM–Newton* high-luminosity bin with, for example, observation 0111800101 appearing much softer than the other spectra, with a much higher MCD contribution than two of the four other spectra in this bin despite its lower luminosity. Finally, interesting supporting evidence for precession might be provided by the long-term X-ray variability; it has been recently reported by Lin et al. (2015) that Holmberg IX X-1 exhibits a quasi-period of ~ 625 d in *Swift* data, potentially a superorbital period due to the precession of the accretion disc. Hence the predicted changes from this physical process appear largely consistent with the spectral degeneracy that we do see, and are potentially supported by the observed long term X-ray variability, so we infer that precession has an important role in the observed spectrum of this ULX.

5 CONCLUSION

In this paper we have analysed *Swift*, *XMM–Newton* and *NuSTAR* spectra of the archetypal ULX Holmberg IX X-1. The wealth of data, particularly in the form of over 500 observations with *Swift*, has allowed us to study the evolution of the spectra with observed source luminosity. We find that the data tend to evolve from relatively flat spectra in the 1–6 keV range, or two-component spectra that have a classic HUL form at lower luminosities, to a spectrum that is distinctly curved and disc-like at the highest luminosities, with the peak energy in the curved spectrum tending to decrease with increased luminosity. We study the spectra mainly in terms of a two-component model consisting of a cool MCD blackbody and a hotter Comptonized medium (DISKBB + COMPTT in XSPEC), but the requirement for an additional component in *NuSTAR* data, the degeneracy in behaviour of the soft and hard components when other models are used, and the need for the MCD to become substantially brighter and warmer when the disc spectrum gets very curved, dissuades us from directly interpreting the changes in individual model components. Instead, we discuss the changes in the overall spectral shape in terms of physical models. We argue that a 'slim disc' model can produce the apparent cooling in the spectra at higher luminosities, if it is viewed at high inclination. However, other studies argue that Holmberg IX X-1 is viewed close to face on, and a relative lack of variability below 1 keV, compared to above, is not expected for a pure disc model. Instead, a supercritical accretion disc with a massive, radiatively driven wind appears likely to be able to explain the main characteristics of the spectral evolution, with the cooling occurring due to Compton down-scattering in the wind as it expands and starts to cross the line of sight at the highest accretion rates. The relatively higher increase in flux above 1 keV is then due to beaming of the hard emission from the inner disc up the 'funnel' structure bounded by the disc and the massive, optically thick wind. The remaining characteristic of the data – a degree of degeneracy between different spectra observed at the same luminosity – can be explained if the ULX does not remain at a fixed inclination to the line of sight, but instead the BH rotational axis precesses.

The analysis in this paper adds to the growing body of evidence that many ULXs are likely to be sMBHs accreting at super-Eddington rates, where their observational properties can be explained by the distinct geometry produced by the combination of the large scaleheight disc, and the massive, outflowing wind. The supposition that this geometry changes in response to the accretion rate means that our view of this phenomenon is driven by two main factors: the accretion rate, and the inclination of the BH axis to our line of sight. In the case of Holmberg IX X-1 we argue that the range of spectra seen, and particularly the degeneracy with luminosity, mean that both these parameters vary in the ULX; we see the ULX precess, as is seen in the Galactic BH SS433. So, our understanding of the ULX phenomenon continues to grow. However, many questions remain, not least the details of the exact geometry of the disc and outflowing wind (if this is indeed the correct model for ULXs), and the state of the material in it. The answers to some at least of these questions may be accessible in the future if a calorimeter detector is successfully flown, the potential high resolution and large collecting area of which would be ideal for detecting narrow emission and/or absorption feature in the ULX winds, if they are present.

ACKNOWLEDGEMENTS

We thank the anonymous referee for their comments, that have helped improve this paper. WL acknowledges financial support in the form of funding for a PhD studentship from the Royal Thai Government. TPR and CD thank STFC for support as part of the consolidated grant ST/L00075X/1. We also would like to thank Matthew Middleton and Dominic Walton for helpful discussions. This work is in part based on observations obtained with

XMM–Newton, an ESA science mission with instruments and contributions directly funded by ESA Member States and NASA. This research has also made use of data obtained with *NuSTAR*, a project led by Caltech, funded by NASA and managed by NASA/JPL, and has utilized the NUSTARDAS software package, jointly developed by the ASDC (Italy) and Caltech (USA).

REFERENCES

Bachetti M. et al., 2013, ApJ, 778, 163
Bachetti M. et al., 2014, Nature, 514, 202
Berghea C. T., Dudik R. P., Tincher J., Winter L. M., 2013, ApJ, 776, 100
Caballero-García M. D., Fabian A. C., 2010, MNRAS, 402, 2559
Colbert E. J. M., Mushotzky R. F., 1999, ApJ, 519, 89
Dewangan G. C., Griffiths R. E., Rao A. R., 2006, ApJ, 641, L125
Dewangan G. C., Jithesh V., Misra R., Ravikumar C. D., 2013, ApJ, 771, L37
Dickey J. M., Lockman F. J., 1990, ARA&A, 28, 215
Fabbiano G., 1988, ApJ, 325, 544
Fabrika S., 2004, Astrophys. Space Phys. Rev., 12, 1
Fabrika S., Ueda Y., Vinokurov A., Sholukhova O., Shidatsu M., 2015, Nature Phys., 11, 551
Farrell S. A., Webb N. A., Barret D., Godet O., Rodrigues J. M., 2009, Nature, 460, 73
Feng H., Soria R., 2011, New Astron. Rev., 55, 166
Gladstone J. C., Roberts T. P., Done C., 2009, MNRAS, 397, 1836
González-Martín O., Papadakis I., Reig P., Zezas A., 2011, A&A, 526, A132
Grisé F., Kaaret P., Feng H., Kajava J. J. E., Farrell S. A., 2010, ApJ, 724, L148
Grisé F., Kaaret P., Pakull M. W., Motch C., 2011, ApJ, 734, 23
Heil L. M., Vaughan S., Roberts T. P., 2009, MNRAS, 397, 1061
Hui Y., Krolik J. H., 2008, ApJ, 679, 1405
Kaaret P., Feng H., 2009, ApJ, 702, 1679
Kajava J. J. E., Poutanen J., 2009, MNRAS, 398, 1450
Kajava J. J. E., Poutanen J., Farrell S. A., Grisé F., Kaaret P., 2012, MNRAS, 422, 990
Kawashima T., Ohsuga K., Mineshige S., Yoshida T., Heinzeller D., Matsumoto R., 2012, ApJ, 752, 18
King A. R., 2009, MNRAS, 393, L41
Kong A. K. H., Yang Y. J., Yen T.-C., Feng H., Kaaret P., 2010, ApJ, 722, 1816
La Parola V., Peres G., Fabbiano G., Kim D. W., Bocchino F., 2001, ApJ, 556, 47
Lin L. C.-C., Hu C.-P., Kong A. K. H., Yen D. C.-C., Takata J., Chou Y., 2015, MNRAS, 454, 1644
Liu J.-F., Bregman J. N., 2005, ApJS, 157, 59
Liu J.-F., Bregman J. N., Bai Y., Justham S., Crowther P., 2013, Nature, 503, 500
Marlowe H. et al., 2014, MNRAS, 444, 642
Mezcua M., Roberts T. P., Lobanov A. P., Sutton A. D., 2015, MNRAS, 448, 1893
Middleton M. J., Roberts T. P., Done C., Jackson F. E., 2011, MNRAS, 411, 644
Middleton M. J., Walton D. J., Roberts T. P., Heil L., 2014, MNRAS, 438, L51
Middleton M. J., Heil L., Pintore F., Walton D. J., Roberts T. P., 2015a, MNRAS, 447, 3243
Middleton M. J., Walton D. J., Fabian A., Roberts T. P., Heil L., Pinto C., Anderson G., Sutton A., 2015b, MNRAS, 454, 3134
Miller J. M., Fabbiano G., Miller M. C., Fabian A. C., 2003, ApJ, 585, L37
Miller J. M., Fabian A. C., Miller M. C., 2004, ApJ, 614, L117
Miller J. M., Walton D. J., King A. L., Reynolds M. T., Fabian A. C., Miller M. C., Reis R. C., 2013, ApJ, 776, L36
Miller J. M., Bachetti M., Barret D., Harrison F. A., Fabian A. C., Webb N. A., Walton D. J., Rana V., 2014, ApJ, 785, L7
Mitsuda K. et al., 1984, PASJ, 36, 741
Motch C., Pakull M. W., Soria R., Grisé F., Pietrzyński G., 2014, Nature, 514, 198
Ohsuga K., Mineshige S., 2011, ApJ, 736, 2
Pintore F., Zampieri L., 2012, MNRAS, 420, 1107
Pintore F., Zampieri L., Wolter A., Belloni T., 2014, MNRAS, 439, 3461
Poutanen J., Lipunova G., Fabrika S., Butkevich A. G., Abolmasov P., 2007, MNRAS, 377, 1187
Roberts T. P., 2007, Ap&SS, 311, 203
Roberts T. P., Gladstone J. C., Goulding A. D., Swinbank A. M., Ward M. J., Goad M. R., Levan A. J., 2011, Astron. Nachr., 332, 398
Sazonov S. Y., Lutovinov A. A., Krivonos R. A., 2014, Astron. Lett., 40, 65
Steiner J. F., Narayan R., McClintock J. E., Ebisawa K., 2009, PASP, 121, 1279
Stobbart A.-M., Roberts T. P., Wilms J., 2006, MNRAS, 368, 397
Sutton A. D., Roberts T. P., Walton D. J., Gladstone J. C., Scott A. E., 2012, MNRAS, 423, 1154
Sutton A. D., Roberts T. P., Middleton M. J., 2013, MNRAS, 435, 1758
Sutton A. D., Done C., Roberts T. P., 2014, MNRAS, 444, 2415
Sądowski A., Narayan R., 2016, MNRAS, 456, 3929
Tagliaferri G. et al., 2004, in Flanagan K. A., Siegmund O. H. W., eds, Proc. SPIE Conf. Ser. Vol. 5165, X-Ray and Gamma-Ray Instrumentation for Astronomy XIII. SPIE, Bellingham, p. 241
Takeuchi S., Ohsuga K., Mineshige S., 2013, PASJ, 65, 88
Takeuchi S., Ohsuga K., Mineshige S., 2014, PASJ, 66, 48
Titarchuk L., 1994, ApJ, 434, 570
Vierdayanti K., Mineshige S., Ebisawa K., Kawaguchi T., 2006, PASJ, 58, 915
Vierdayanti K., Done C., Roberts T. P., Mineshige S., 2010, MNRAS, 403, 1206
Vierdayanti K., Sadowski A., Mineshige S., Bursa M., 2013, MNRAS, 436, 71
Walton D. J., Miller J. M., Reis R. C., Fabian A. C., 2012, MNRAS, 426, 473
Walton D. J., Miller J. M., Harrison F. A., Fabian A. C., Roberts T. P., Middleton M. J., Reis R. C., 2013a, ApJ, 773, L9
Walton D. J. et al., 2013b, ApJ, 779, 148
Walton D. J. et al., 2014, ApJ, 793, 21
Walton D. J. et al., 2015, ApJ, 806, 65
Wang Q. D., Yao Y., Fukui W., Zhang S. N., Williams R., 2004, ApJ, 609, 113
Wilms J., Allen A., McCray R., 2000, ApJ, 542, 914
Winter L. M., Mushotzky R. F., Reynolds C. S., 2006, ApJ, 649, 730
Winter L. M., Mushotzky R. F., Reynolds C. S., 2007, ApJ, 655, 163
Zampieri L., Roberts T. P., 2009, MNRAS, 400, 677

SUPPORTING INFORMATION

Additional Supporting Information may be found in the online version of this article:

Appendix A
(http://www.mnras.oxfordjournals.org/lookup/suppl/doi:10.1093/mnras/stw1282/-/DC1).

Please note: Oxford University Press is not responsible for the content or functionality of any supporting materials supplied by the authors. Any queries (other than missing material) should be directed to the corresponding author for the article.

This paper has been typeset from a TEX/LATEX file prepared by the author.